DESIGN AND MODELING OF A SOFT, PRESSURISED, SPHERICAL ROBOT

A Thesis

by

MEGHALI PRASHANT DRAVID

Submitted to the Graduate and Professional School of
Texas A&M University
in partial fulfillment of the requirements for the degree of

MASTER OF SCIENCE

Chair of Committee,	Robert Ambrose
Committee Members,	Swaroop Darbha
	Manoranjan Majji
Head of Department,	Guillermo Aguilar

December 2022

Major Subject: Mechanical Engineering

ABSTRACT

In the world of spherical robots groundbreaking innovations with regards to the sensory system and driving mechanism have taken place in last few decades. The motivation in this thesis is to integrate these innovations and develop a spherical robot, "RoboBall", with a novel elastic spherical shell. This thesis reports on the design of the elastic shell, the modeling of robot's dynamics and comparison of the analytics with experimental results. In addition to the electric motor-powered motion of the ball, the robot is also able to adjust its air pressure with an embedded pneumatic control system, and this thesis shows how that causes changes in the ball's dynamics. The design of the internal driving mechanism, prior history, and a taxonomy of the spherical robots is also outlined. A non-trivial feature of the robot is its soft and pressure controlled elastic shell, which presented numerous design challenges. The rigid endplates and elastic exterior together form the skin of the robot, and different elastic-rigid interfaces for an air-tight robot are explored. The development of the internal pressure control system and its components are discussed. The "RoboBall" has an internal pendulum driven mechanism. The pendulum has two degrees of freedom; rolling and steering. A motion in the third direction i.e., oscillation in the vertical direction, is not actively controlled by the pendulum or any other mechanism but is governed by the system's dynamics. This study focuses on the third degree of freedom, the bouncing of the "RoboBall", which can be affected by varying the pressure inside the ball. The bouncing of the ball is modeled as a simplified spring-mass damper system and the effect of variation of pressure on different parameters. The thesis concludes with an experimental evaluation of a mass equivalent system, and comparison of these results to the formulated dynamic model.

ACKNOWLEDGEMENTS

CONTRIBUTORS AND FUNDING SOURCES

Contributors

This work was supported by a thesis committee consisting of Professor Dr. Robert Ambrose and Dr. Swaroop Darbha of the Department of Mechanical Engineering, TAMU and Professor Dr. Manoranjan Majji of the Department of Aerospace Engineering, TAMU.

All the work conducted for the thesis was completed by the student independently.

Funding sources

<center>NOMENCLATURE</center>

COR	Coefficient of Restitution
DOF	Degrees of Freedom
BSR	Barycentric Spherical Robots
UAV	Unmanned Aerial Vehicles
R_{ball}	Radius of the ball robot
m	Mass of the ball
g	Gravitational acceleration
R_{cg}	Radius of Center of Gravity
θ	Angle of Slope
h	Step Height
y	Vertical Compression of the sphere
w	Thickness of the sphere
$A(y)$	Surface area in contact with ground during compression
$V(y)$	Volume of the sphere after compression
$r(y)$	Radius of the surface in contact with ground
$\theta(y)$	Angle between horizontal and tangent to the sphere at point of contact
P_g	Gauge Pressure inside the Robot
P_i	Absolute Internal Pressure
P_o	Absolute Pressure outside sphere

<center>v</center>

P_y	Internal Pressure after compression
F_r	Restoring force due to change in Pressure
F_s	Restoring force due to shear stain in the material
τ	Shear Stress
G	Shear Modulus
K_i	Initial Kinetic energy
F_d	Dissipative Force
DCV	Directional Control Valves
V_{ball}	Volume of the hollow robot
$V_{pendulum}$	Volume of the Pendulum
V_{air}	Volume of the robot consisting of only air
V_{tank}	Volume of the hollow tank
k	Linear Stiffness
c	Viscous damping
ω_n	Natural Frequency
ω_d	Damping Frequency
ζ	Damping Ratio
e	Coefficient of Restitution
δT	Contact time
h_i	Drop Height
v_i	Velocity of ball before impact

x	Vertical distance from ground to the center of the ball
h_k	Height attained by the ball after k^{th} bounce
T_{total}	Total time elapsed
n	Number of Bounces
e	Coefficient of Restitution
T_{air}	Flight time
$T_{contact}$	Total Contact time
pen	Vertical robot penetration in the ground

TABLE OF CONTENTS

LIST OF FIGURES

LIST OF TABLES

CHAPTER I: INTRODUCTION

Spherical robots are a special kind of mobile robot. These are generally described by an external spherical shell with an internal driving mechanism, which allows active steering and control. Spherical robots provide an alternative solution to conventional wheeled vehicles. As one would expect, primary locomotion of a spherical robot is rolling, although other functionalities such as jumping, and hopping are also possible. Spherical robots have been keenly studied and developed for a wide range of application from toys to rovers, as reviewed in Chapter II.
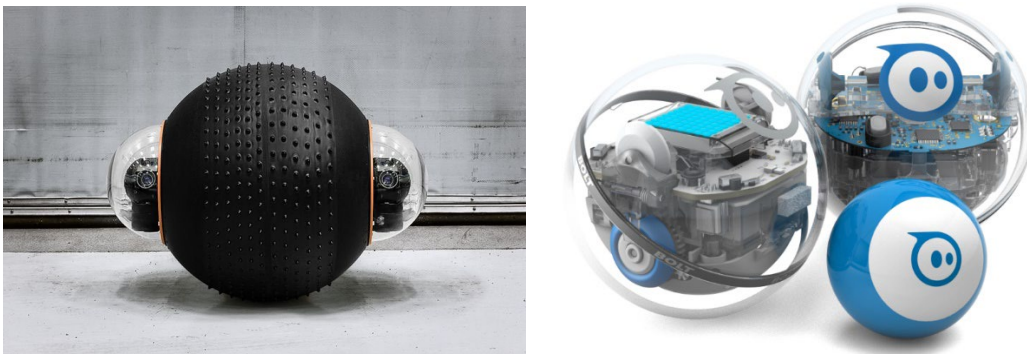
Figure 1 Examples of Spherical Robot

The spherical robot in this thesis is inspired by the challenge of roving on the moon. This robot, named "*Roboball*", is a pendulum driven, 24" in diameter, spherical robot with a pressurized and flexible shell. Unlike conventional 4 wheeled or 6 wheeled rovers the spherical robot cannot flip over or fall down. Consequently, the top speed of a wheeled rover is much slower than a spherical robot. This unique advantage makes the *Roboball* suitable for travelling down into craters

on the moon, where a wheeled robot is likely to flip. In addition, as the robot is inside an exterior shell the "electronic/robot components are protected from the harsh thermal environment and dust particles. These characteristics makes it a perfect fit for operating in extreme terrain.
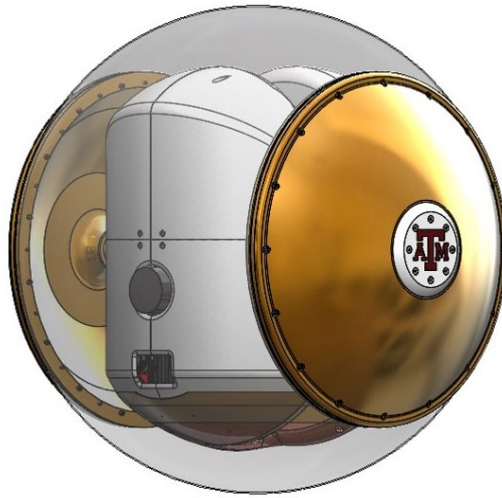
Figure 2 RoboBall

This thesis discusses the design and development of the "Roboball" from the ground up. The modern pneumatic tire enables land vehicles to maintain optimal ground pressure and traction while tolerating rocky terrain and varying levels of soft soils. Separating tires across a wheelbase, vehicles can apply torque to ground traction, but with the complexity of steering, suspension, and other mechanisms that mount those multiple tires to a central chassis. The robot described here has only a single, spherical wheel: it is simply a ball. The parametric model of the robot is presented in Chapter III, with design parameters related to performance measures such as top speed, hill, and step climbing. Chapter III also includes a detailed description of the various sub systems and their functionality in the robot.

A sizeable amount of work has been done in kinematic and dynamic modelling, control, and path planning of ball-shaped robots with different constructions. Some balls are driven by external forces like gravity or wind. Others move due to internal motion of their center of gravity, and these are called barycentric spherical robots (BCR's). Designs for moving BCR's internal center of gravity include tracked vehicles rolling inside the ball (aka Hamster ball), use of internal cables, use of flywheels, use of 1 or 2 pendula, and mixes of these approaches. A taxonomy of spherical balls will be developed in Chapter II.

The 2 Degrees of Freedom (DOF) pendulum-driven type appears to be one of the favored forms of propulsion. Typically, the degrees of freedom are implemented as two perpendicular and intersecting joint axes in the center of the ball. Other designs use a clever arrangement of two 1 DOF pendula to achieve instantaneous turning [1]. Pendulum driven types show abilities to climb slopes [2] and follow paths [3]. However, most of these systems are comprised of a hard outer shell not suitable to off-road terrain. One team developed a flexible shell based on flexible rods arranged in a sphere to help with collision tolerance [4], yet the flexible shell was purely for impact mitigation and its effect on the ball dynamics were not considered. All robots presented here were studied with a dynamic model. This model was derived from a 2 DOF Lagrangian approach. Either PID or fuzzy controllers were used to control either torque or position, often using video as feedback. The extensive previous art related to spherical robots which is discussed in Chapter II.

The novelty of the robot is its soft and flexible external shell; hence the system is pressurized. In addition, the robot has an internal pneumatic system which allows it to change the internal pressure during rolling. When an off-road vehicle is driven on sand the tires need to be aired down for optimal performance, while on asphalt the tires need to be aired up. This change in internal pressure is non-trivial for performance. RoboBall is able to adapt internal pressure with

an embedded pneumatic control system that moves air between the inflatable ball and internal high-pressure storage tanks, or back.

The variable pressure characteristics of the robot can be used to detect unknown terrain as well. The robot will have a its own bouncing natural frequency and the hypothesis is that at different pressure the bouncing frequency and damping changes. To verify the hypothesis and experimental study is carried out with different internal pressure to analyze the bouncing ball behavior as a function of pressure change as it bounces. This thesis presents a simplified model for the bouncing ball. This bouncing ball model is represented as a spring-mass- damper system. A MATLAB model was developed and validated with experimental results.

The behavior of a bouncing ball is a classic problem in physics and dynamics textbooks. These books address the concept of mass, stiffness, and damping as elemental properties of the mechanical system. In one example, M. Nagurka and S. Hung present a bouncing ball system as a linear mass-spring-damper model for a ping pong ball [5]. Though this model well describes the impact of damping ratio, stiffness constant, and damping constant on the system's coefficient of restitution for small-size applications, the study does not analyze the effect of pressure changes inside the ball. Surprisingly, no simple, mechanistic model describing the relation between internal ball pressure and bouncing coefficient of restitution is found until 2015 when Georgallas and Landry formulated a model considering the pressure changes and dissipative energy during bouncing and relating both to the coefficient of restitution [6]. In this referenced work the behavior of the bouncing ball is modeled based on the energy conservation principle. Martin and Bruce Allen conducted a study of energy loss of bouncing tennis balls as a function of temperature induced changes in pressure [7]. In these cases, the mass modeled was in the ball membrane,

distributed around the perimeter surface of the sphere, whereas RoboBall has a significant additional mass inside the ball on the pendulum.

CHAPTER II: LITERATURE REVIEW

The spherical robots have been studied for over more than a century. This chapter introduces different spherical robots and their different mechanical construction. The study here focuses on the robots moving on terrain with internal power and traction to the ground. Wind-propelled balls, floating and flying ball robots are also presented as a curiosity. Finally, this chapter discusses the existing study of flexible and rolling balls along with the dynamic models of pressurized balls.

Taxonomy of the Ball Robots

Spherical robots can be classified into different categories, primarily sorted by the method of actuation of the ball. In recent years "Barycentric Spherical Robots" (BSR) have become the prominent area of study for self-propelled systems, moving due to a non-collocated center of mass. Wind driven spherical robots have been studied with limited application because of their parameter complexities and passive nature. Different propulsion mechanisms have been explored for the application of spherical geometry in UAVs and underwater vehicles. The BSRs are most commonly driven on the ground motion. They rely on non-collocated center of mass and center of rotation to generate propulsion. Pendulum driven, wheel based and sliding mass mechanism all come under BSR tree of ball categories. Earlier in the robot development spring actuated mechanisms and human-carrying spherical vehicles were attempted and will be discussed later in this chapter. The robots can be classified on the method of control and active degrees of freedom, such as, only forward rolling, curved path, oscillating path, reactive change of rolling direction, reactive activation of steering function, or two degrees of freedom. Subsequently, the robot can be classified based on the steering method, for instance, tilting of rolling axis, inertia steering, internal

movable rolling axis, or multiple moving masses. With this work a new category for sorting is proposed, described by rigid or flexible shells.

Early 1-Dof Models

The earliest spherical ball that carries an internal one degree of freedom counter mass, the 'Toy' was developed by J.L Tate, patented in U.S. in 1893 (U.S. Patent 508,558) and is a BSR type design. The toy was constructed in a manner where the central axis carried the counter mass and had an elastic spring and a drum that winds the spring when the ball is first manually rotated, figure 3 illustrates the design. The elastic spring actuated toy would roll in the forward direction upon the release of the ball due to the unwinding of the spring from the drum. There is no active steering. Several other patents were approved later which modified the internal mechanical construction of the spring but operated on the same principle. One of the more complex designs includes a clock-spring along with a gearbox.
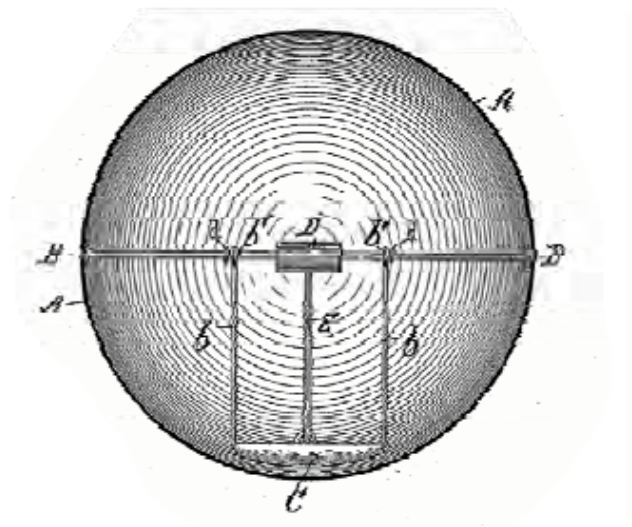
Figure 3 Toy by J.L. Tate (U.S. Patent 508,558)
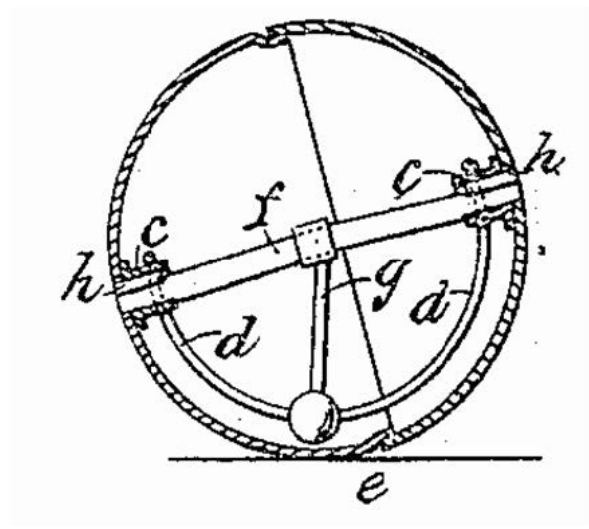
Figure 4 Self-Propelling Device by B. Shorthouse (U.S. Patent 819,609)

The next significant development was made in 1906, when B. Shorthouse (U.S. Patent 819,609) proposed an opportunity to manually adjust the position of an internal counterweight, thus causing a curved trajectory for a ball rolling rather than a straight path. Figure 4 shows the tilted arrangement relative to horizontal of the counter-mass and support which can be adjusted manually. Mechanisms producing irregular rolling paths for self-propelled balls were then patented. E.E Cecil used a gear arrangement to shift the counter-mass inside the sphere (U.S. Patent 933,623) with a ball that follows a zig-zag path due to continuous change in attitude of the rolling axel prompted by the motion of the internal counter-mass. Figure 5 describes the mechanical toy.
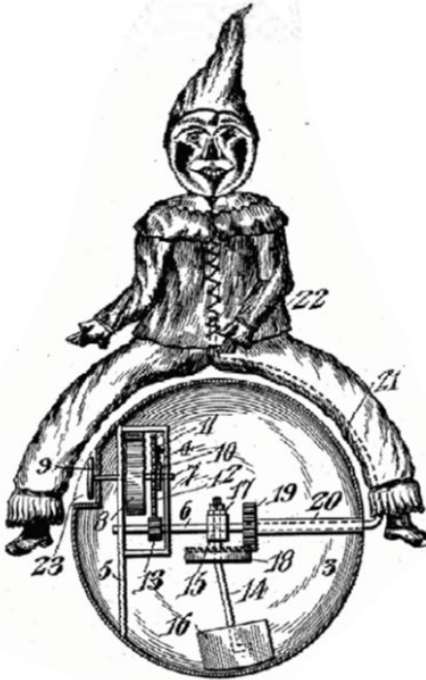
Figure 5 Mechanical Toy by E.E. Cecil (U.S. Patent 933,623)

A spherical vehicle able to carry a man in a similar BSR manner was first developed for marine applications in 1889. W. Henry proposed this vehicle (U.S Patent 396,486) for floating on water, with the passenger weight and a ballast mass balancing the vehicle. A hand operated crank was producing the driving force while the steering was achieved by the passenger moving his or her weight inside the vehicle (figure 6). Ever since, many patents have been published where a person would ride inside the spherical vehicle and operate it. A few examples are mentioned here. J.E Reilley patented a ball shaped car in 1941 (Figure 7). In 1958, the vehicle was operated directly without any additional mechanism like a hamster inside a treadmill. (Figure 8). In 1969, E. Cloud developed an inflatable/deflatable design which could be carried and stored easily, though not much attention was paid to the mobility (U.S Patent 2,838,022). A pedal mechanism used both on land and water shown in figure 10 was created in 1980 by C. Maplethorpe and K. E. Kary (U.S

Patent 3,428,015). Steering was done by the person shifting the center of gravity similar to operating hang-gliders (figure 11) in a patent by L.R Clark Jr. and H.P. Greene Jr. (U.S. Patent 4,386,787). An open mesh spherical structure (figure 12) was presented by J.S. Sefton (U.S. Patent 4,501,569). A complex drive mechanism is illustrated in figure 13, with tracks composed of multiple wheels coordinated inside the shell to control the rolling direction. This design was developed in 1971 by A. Ray (U.S. Patent 4,729,446).
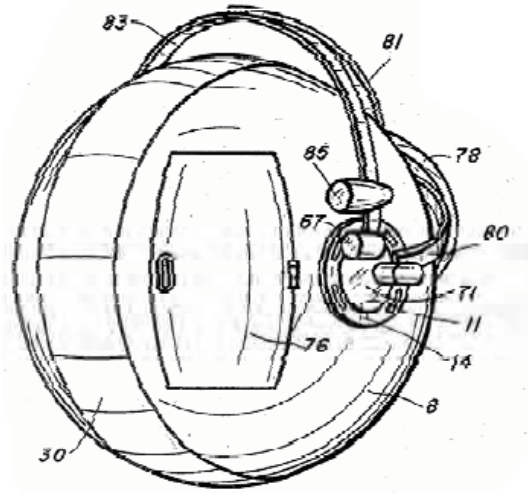
Figure 6 Marine vessel by W. Henry (U.S. Patent 396,486)
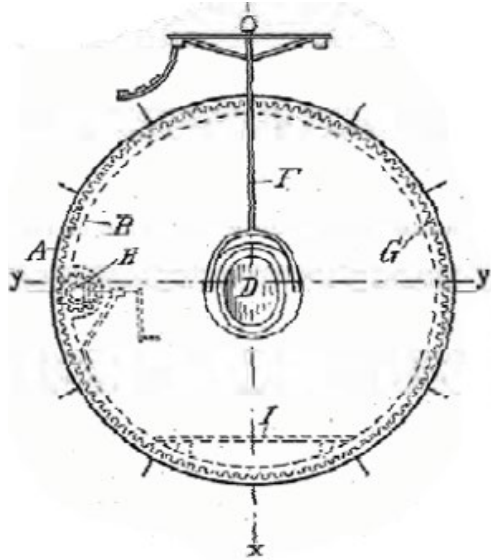
Figure 7 A spherical vehicle by J.E. Reilley (U.S. Patent 2,267,254)
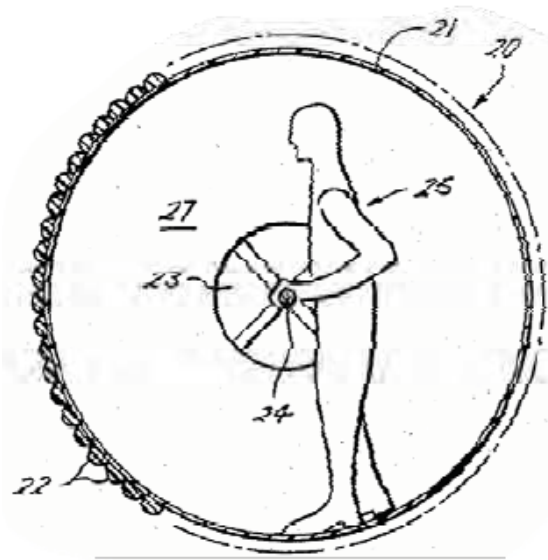
Figure 8 Spherical vehicle by S. E. Cloud (U.S. Patent 3,428,015)
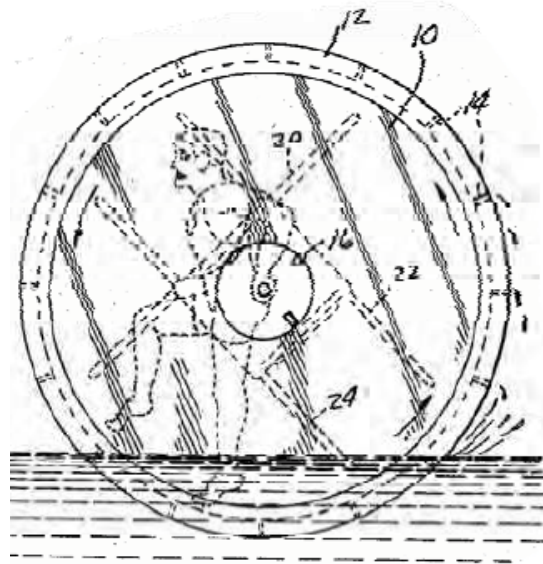
Figure 9 Spherical water craft by W. E. Wilson (U.S. Patent 2,838,022)
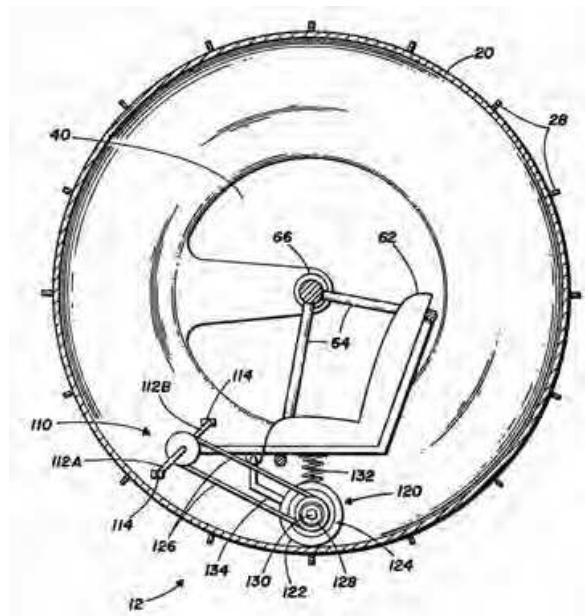
Figure 10 Spherical vehicle by C. Maplethorpe and K. E. Kary (U.S. Patent 4,386,787)
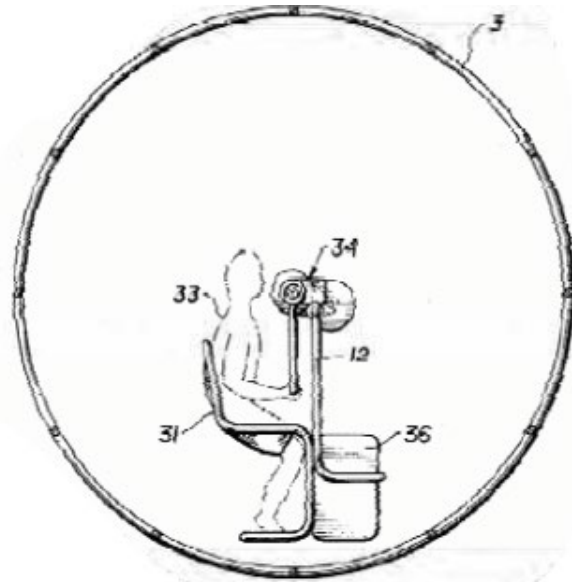
Figure 11 Spherical vehicle by L. R. Clark Jr. and H. P. Greene Jr. (U.S. Patent 4,501,569)
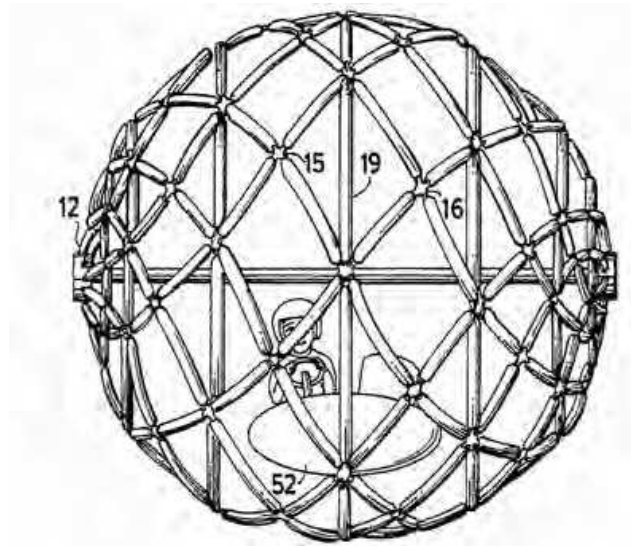
Figure 12 Mobile sphere by J.S. Sefton (U.S. Patent 4,729,446)
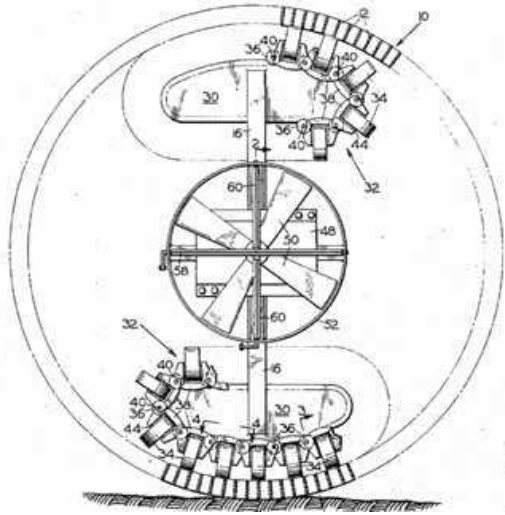
Figure 13 Spherical vehicle by A. Ray (U.S. Patent 3,746,117)

Two very consecutive patterns, first by J.M. Easterling in 1957 (U.S. Patent 2,949,696) and second by E.A.Glos in 1958 (U.S. Patent 2,939,246), replaced the mechanical spring power source with a battery and an electric motor. The later of the two designs had a gravity-operated switch for activating and deactivating the motor in preferred angular position. Easterling put forwarded autonomously reversing of the ball for half a revolution when the motor drives the counterweight over the upper dead center. He noted the direction of the ball can also be changed, which allows the ball to move continuously. Some of the newer toys such as 'Weaselball', 'Squiggleball' and 'Robomaid' were patented based on the basic principle used by Easterling.
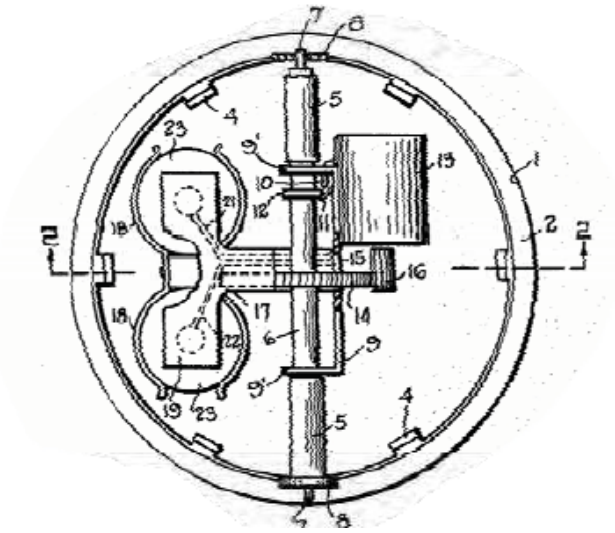
Figure 14 Toy ball by E. A. Glos (U.S. Patent 2,939,246)
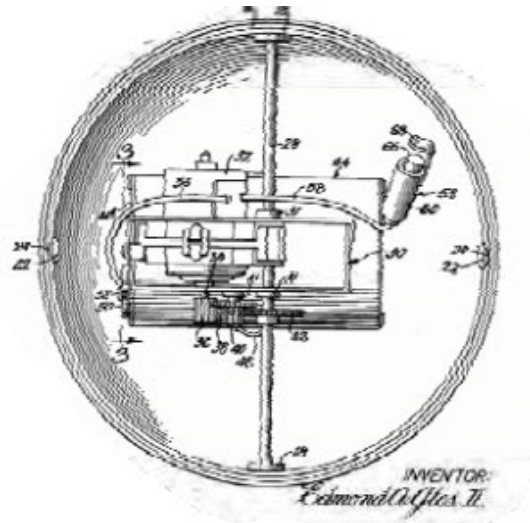
Figure 15 Toy by J. M. Easterling (U.S. Patent 2,949,696)

The modern day "Squiggle ball" design is similar to the Easterling design. An addition to the earlier design is a new rubber band on the outer circumference of the ball to add friction to the floor and facilitating the rolling axis tilting one way or the other. This change causes the rolling of the ball along slightly curved paths as well as autonomous reversing. Hence, the ball does not get

15

stuck in the corners. Later innovations coupled the electric motors with different mechanical mechanisms and other technological developments like sensing with mercury switches and adding light and sound effects for appearance or communication.

Figure 16 'Squiggleball' opened to show the interior parts
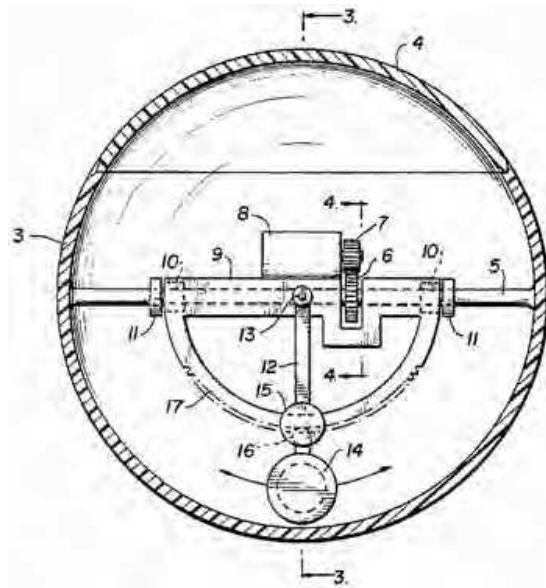
Figure 17 Steerable ball toy by L. R. Clark Jr. et al. (U.S. Patent 4,501,569)
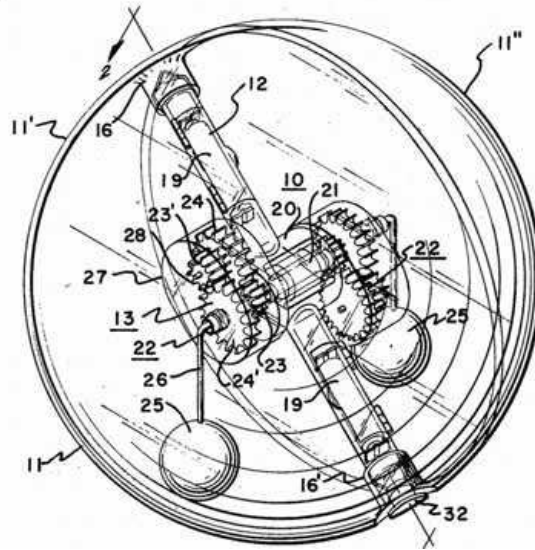
Figure 18 Motor driven ball toy by McKeehan (U.S. Patent 3,798,835)

McKeehan introduced the active and controlled second degree of freedom for the first time in 1974 (U.S. Patent 3,798,835). Rather than a rolling axis across the ball, he introduced a support post which carried the rotating counterweights in the center making the rolling axis perpendicular to the post. The post itself is connected to the shell, thus its ends are on the rolling circumference. The mass is divided into two halves representing two pendulums as a consequence of the rotating post in the middle of the ball. These two splits (but kinematically connected) pendula denote the first degree of freedom, which is actuated with a single electric motor. It has an inertial switch to change the rolling direction. The second degree of freedom, and a second electric motor, causes a steering rotation around the longitudinal axis of the post. Figure 18 illustrates the McKeehan's design. Leaning left or right, the horizontal position of the post while spinning would make the ball roll sideways. Similarly. The vertical position of the post while spinning will cause a change in the rolling direction. Irregular motion is generated with combined motion of the post and pendulum along with the position of the post.

17

Hamster Ball

An alternative mechanism, spring-driven hamster-ball was patented by A.D McFaul in 1918, which utilized the friction between the inner surface of the sphere and the traction wheels mounted on the counter-mass for the motion of the ball. This design is known for its low torque needed for driving and is another form of the BSR category of balls since the total system mass is offset from the axis of rotation. In pendulum designs a leaver arm is used to support the counterweight and the counter-mass movement inside the ball, which requires high torque, and consequently, higher power at stall. In the traction wheel design, the torque required is not based on the length of the lever but instead the diameter of the traction wheel which is significantly less than the lever arm design. This category of BSR's is a subcategory called "Internal Drive Units" or IDU's. Figure 19 shows McFaul's design, with two traction wheels on a single axis supported by the rolling axis. In 1973, C.E. Merril, replaced the two-wheel mechanism with a three-wheel vehicle inside the ball, illustrated in the figure 20. Thereafter, multiple patents were filed for three-wheeled and four-wheeled vehicles inside the ball.
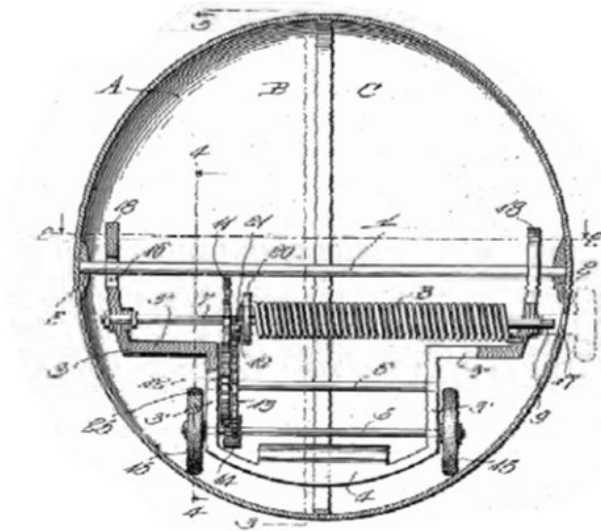
Figure 19 Early hamster-ball by A.D. McFaul (U.S. Patent 1,263,262)
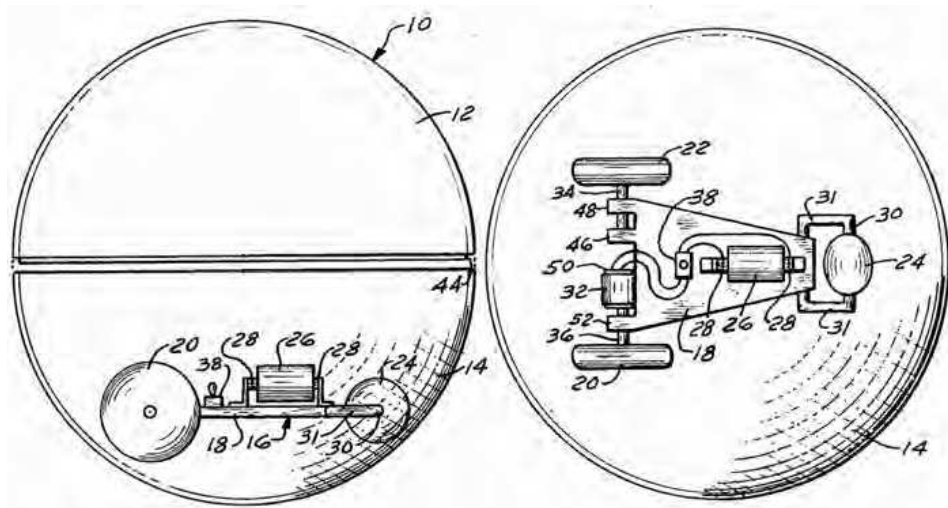
Figure 20 A three-wheeler hamster-ball by C. E. Merril et al. (U.S. Patent 3,722,134)

The next key feature of the spherical robot is its steering capability. Figure 21 illustrates using an advanced radio-controlled 4-wheeled vehicle acting like a hamster in a ball. Figure 23

shows single and two-wheeled radio-controlled robots. Figure 22 presents steerability in the older

two-axis mechanism.
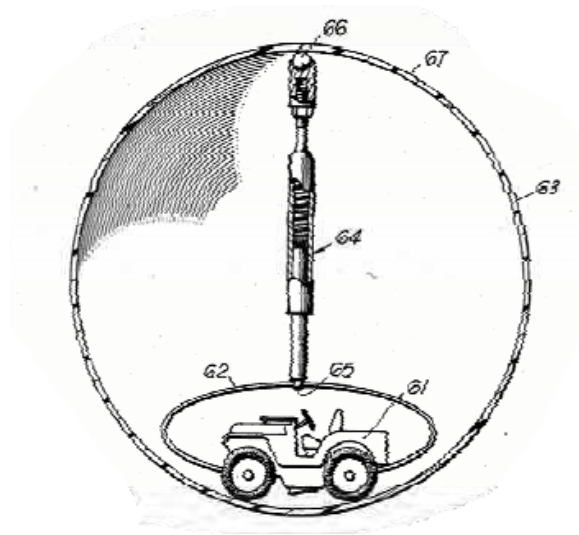
Figure 21 Mechanised toy ball by D. E. Robinson (U.S. Patent 4,601,675)
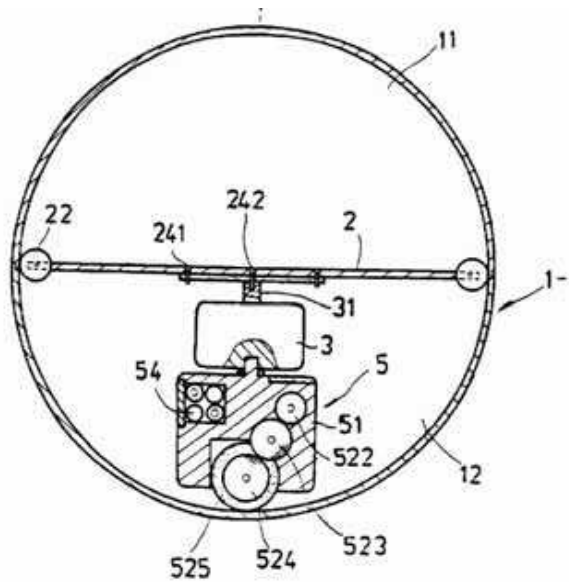
Figure 22 Spherical steering toy by W-M Ku (U.S. Patent 5,692,946)
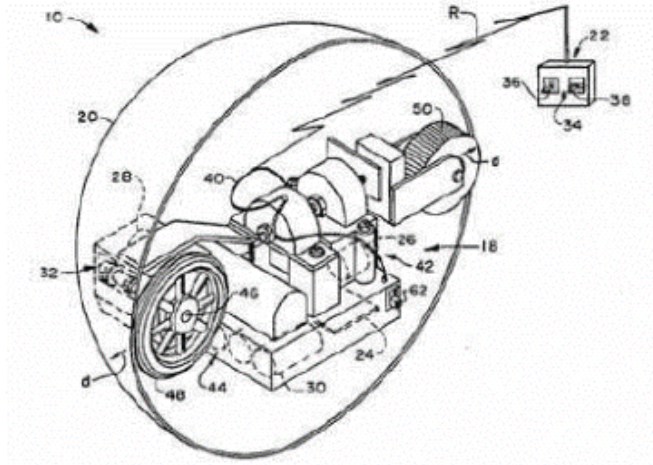
Figure 23 Radio-controlled vehicle within a sphere by J. E. Martin (U.S. Patent 4,541,814)
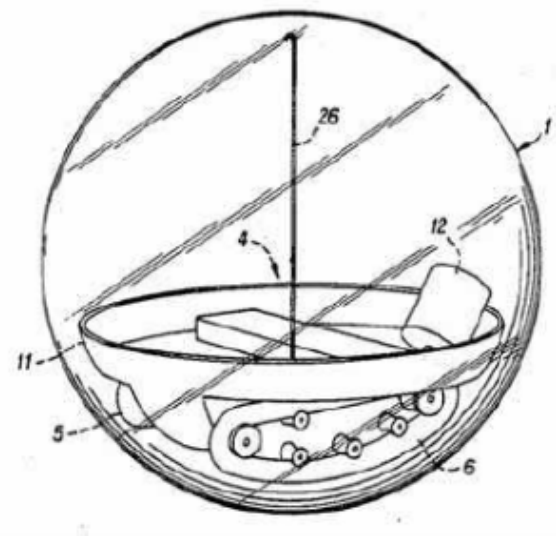
Figure 24 spherical toy by H.V. Sonesson (U.S. Patent 4,927,401)

Wind-Propelled Balls

Abas Kanagi put forward a spherical rover for exploring the planet Mars. The design of the

shell consists of small cells which are inflatable and deflatable on command. The deflation of cells

on one side the support area causes instability, rolling the ball in a controlled manner. The application of this robot was to search for traces of water on the Mars surface.

The presence of a CO_2 atmosphere and varying wind conditions were discovered when Viking landers successfully landed and studied the Mars environment. This gave rise to a new potential for wind-driven exploration rovers on Mars, and potentially Titan and Venus. Wind being an inexpensive and unlimited power source it will be suitable for long range and lengthy exploration missions. In 1977, NASA JPL and the university of Paris came up with the first wind-blown Mars ball. Such a ball, carrying some low-mass scientific instruments for measuring atmospheric conditions or suchlike, would be driven freely by the winds on the surface of the Mars. [8]

The Tumbleweed:

The Tumbleweed rover gets its name from the dead sagebrush balls that blow across the desert of the American southwest, spreading seeds as the roll. The Tumbleweed rover is 6m in diameter. The thin Martian air provides sufficient aerodynamic force to propel the Tumbleweed robot through Martian rock fields when the mass of the rover is less than 20 kgs. The ball is anticipated to climb 20^0 slopes with ease at 10 m/s in a wind speed of 20 m/s on a typical Martian afternoon. The earlier studies of this ball equipped with motorized motion and steerable pendula were abandoned due to the required driving torque and extra mass for actuation.

Several organizations, namely, NASA Jet Propulsion Laboratory (JPL), NASA Langley Research Center (LaRC), Texas Technical University (TTL), and the Swiss Federal Institute of Technology, all have adapted a different concept for the construction of the Tumbleweed robot. All these designs sought to exploit wind thrust force for mobility. [9]

The motivation behind the NASA JPL's 1.5m diameter sphere robot, illustrated in figure 25, came when the researcher observed how a broken and loose inflatable wheel maneuvering through rough terrain and climbing slopes. In Earth testing, Tumbleweed traveled 131 km in Greenland over 9 days. Later it traversed 134 km on the south pole in 7 days [10]. A second Greenland test achieved 200 km in 7 days. This field testing verified the practicability of the robot in demanding environments and arduous terrain. Even so, the Tumbleweed robot performance was bounded due to lack of active control causing near random trajectories that would be left to chance.

Figure 25 NASA JPL's Tumbleweed

Likewise, NASA's Langley Research Center (LaRC) developed the concept of "deployable open-structures" [11]. These vehicles have an open external shell which is biomimetically inspired. The shell has pockets, cutouts, and cups to capture the passing breeze. Figure 26 shows the different designs. Multiple prototypes were designed and tested in a wind-tunnel to identify maximum drag coefficient over a large range of orientation.

Figure 26 NASA's LARC deployable open structures

At NASA's Johnson Space Center, Ambrose and Bridgewater developed the first generation of the RoboBall in 2003 [12] This earlier prototype was an inflatable, 2 degrees of freedom BSR style robot with a 40-inch diameter flexible rubber shell. The drive axis had continuous motion of the pendulum with respect to the main drive axle, which was a hollow 3-inch diameter pipe. The steering axis was limited to a +/- 45-degree angle, but able to steer the robot as it rolled forward or backward. Figure 27 shows the exterior of the ball, and an internal image of the pipe and pendulum.

Figure 27 First Generation RoboBall at Johnson Space Center (2003)

The first generation Roboball suffered from several design challenges. First, the rubber ball exterior was only able to tolerate ~0.1 PSI. Consequently, the vertical mode of vibration (bouncing) was very low and under damped. The ball was a thin rubber, and in addition to limiting the pressure, it was easily popped. But the main challenge was the open loop control of the steering, which did not account for any wobbling in the ball, and caused instability at speeds over 1m/s. Powerful enough to drive at speeds of up to 5 m/s, it was not able to achieve this speed due to a lack of stability. But the high speed, lightweight, and elegant simplicity of the robot made this a BSR form worth later development using modern methods for stabilization. In particular, it needed a better elastic shell and a high performance IMU not readily available in 2003.

New Art

MorpHex MKI is an unusual spherical robot which has multiple different functionalities. Each leg/petal has 3 degrees of freedom plus the upper and lower sphere have 2 degrees of freedom between hemispheres. The robot can roll down a hill like a sphere, it can roll on flat terrain by radially extending petals propelling it forward, or it can traverse from one point to the other using its legs in a hexapod gate. Figure 28, 29 illustrates the different modes and functions of this hybrid ball/leg robot.

Figure 28 MorpHex Miki in leg operation mode

Figure 29 MorpHex Miki in Spherical mode

An amphibious robot was designed and developed by Huiming Xing et al. in 2021. It has the functionality of crawling on the ground, diving underwater and has launching and landing motions to transition between land and water. Figure 30 illustrates the design. [13]
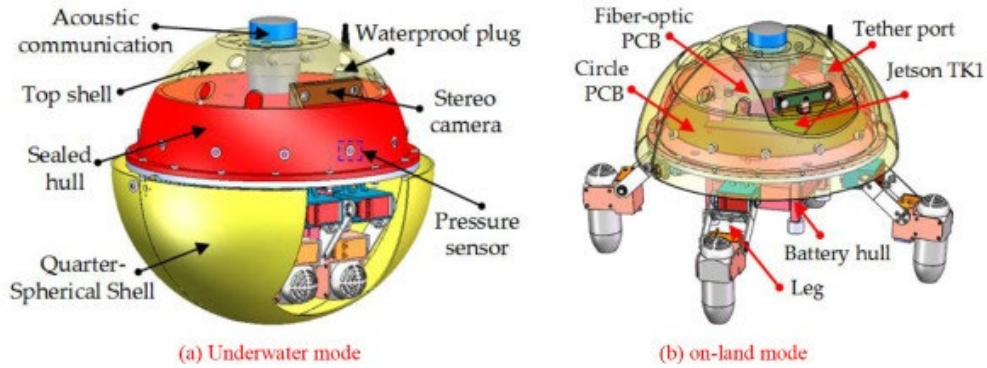
Figure 30 Underwater Spherical robot by Huiming Xing et.al.

Sphero is a commercial toy made by "sphero". It is based on the principle used in the Hamster ball class of BSR's, i.e., it is based on a wheeled IDU (Inertial Drive Unit). The products have LED displays to communicate their state and make the product more attractive. An extensive coding community was developed to help young students learn to program the Sphero with online resources, including the development of phone-based apps for commanding and programming the ball.

Figure 31 Sphero

Samsung has developed a home robot called Ballie. In 2020 Samsung demonstrated their concept, but it has yet to be commercialized. It is presented as a "life companion robot" that "understands you, supports you and reacts to your needs". It has a camera installed for surveillance and personalizing its experience. It is capable of controlling smart home devices and is a friendly toy for the pets, allowing the human owner to monitor pets and the home. Figure 32 shows the Ballie.

Figure 32 Samsung's Ballie

The Japanese Space Agency, JAXA, announced plans to build a transforming lunar rover to explore the moon by transforming its shape. It is being developed for topography and scientific studies of lunar regolith. Figure 33 shows the rover. It is about the size of tennis ball and weighs around 250 gm.

Figure 33 Japanese moon spherical robot

Other Applications

The previous taxonomy of ball robots was restricted to the motion on the ground. Researchers have also been studying and developing applications of the spherical robot off the ground. New developments include underwater spherical robots for monitoring marine environment. The spherical shape allows a robot to be amphibious, walking on land and swimming under water. A design using a simple pump and two fluidic valves to achieve 3-dimensional motions is proposed by Mazumdar et al. 2013 [14] Lin and Guo designed an underwater robot equipped with multiple vectored water jet-based thrusts. Yue et al., in 2015 developed a second-generation SUR II (Spherical Underwater Robot). The underwater robot has 6 degrees of freedom (DOF) which include surge, sway, heave, roll, pitch, and yaw. A hybrid propulsion system was proposed in 2020 by Shuoxin Gu et al. [15]

(a) The 3D model of the SUR II   **(b)** The 3D model of the SUR III
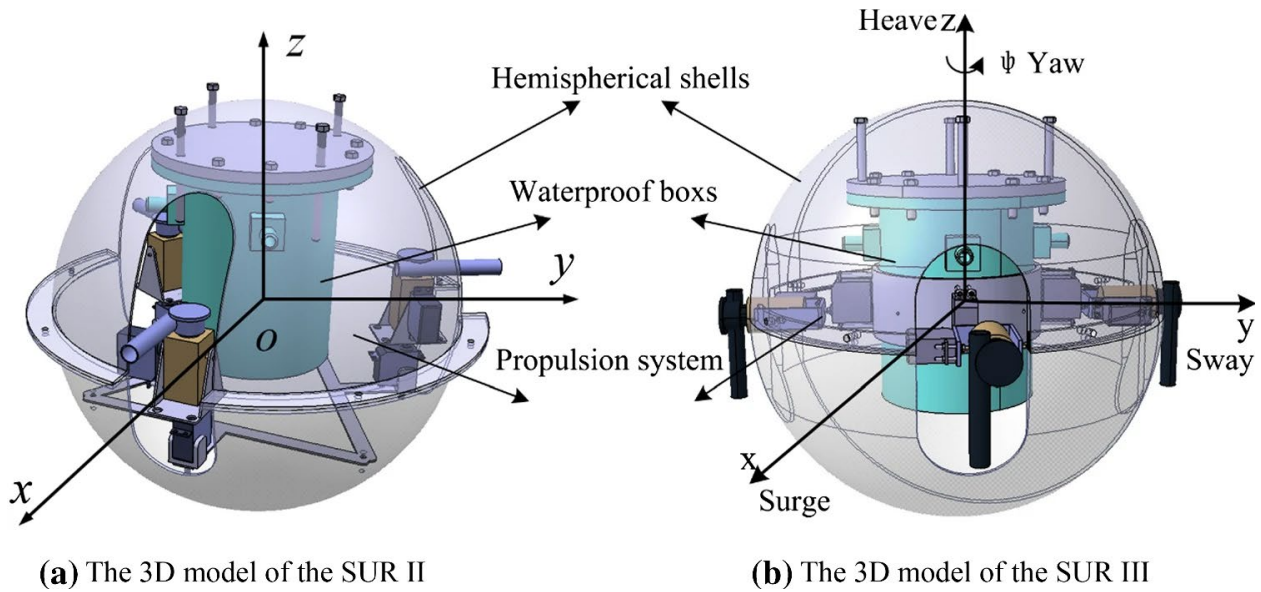
Figure 34 SUR II and SUR III

Gimball, a novel flying spherical robot was developed in the laboratory of EPFL professor Dario Floreano. The objective is to be able to operate where standard robots cannot reach. These 34 centimeters in diameter flying robot is inspired by an insect's resiliency to injury. The exterior spherical shell is an elastic cage like structure that absorbs shocks and rebounds after the collision. Powered by twin propellers and steered by fins, it follows the desired trajectory even after multiple collisions. A gyroscopic stabilization system is used consisting of double carbon-fiber rings, rotating about the robot which maintains a vertical orientation using a drone IMU while the cage rotates and absorbs shocks. The interesting feature of this robot is its ability to navigate impacts using an IMU for stability, which is essential since the lifting propulsion must always be oriented vertically for opposing gravity. Figure 35 shows the Gimball.

Figure 35 Gimball

Similarly, the Kyosho space ball, which is a Japanese toy robot, able to roll on the ground as well as fly in the air. Figure 36 shows the gyroscopically stable egg-shaped toy. K. Malandrakis et al. designed and developed a novel spherical UAVs for operation in complex environment such as buildings, caves or tunnels. Again, the robot uses an IMU to stay oriented vertically.

Figure 36 Kyosho space ball

Figure 37 Example of a flying Spherical Robot

CHAPTER III: SYSTEM DESCRIPTION

As discussed in the previous chapter there is more than one mechanism for a ball robot's locomotion. This chapter describes the selected mechanism for the new version of the RoboBall and different subsystems integrated into the design. The principle of mobility of this robot is based on the BSR style movement of its center of gravity inside the pressurized spherical shell. The goals for this next generation of design are to solve the deficiencies found in the 2003 design's soft elastic ball and the development of an IMU stabilized control for steering. The improvement of the elastic shell, its modeling, experimental evaluation and pneumatic control are the main subject of this Thesis.

Parametric Model

RoboBall's torque is produced about its shaft when the center of gravity moves horizontally away from the centroid. This motion of the center of gravity is caused by moving a 2 degrees of freedom pendulum. The torque produced is transferred to the axle, which is attached to the spherical shell with end plates and ultimately to ground, which causes the ball to roll. The torque generated is directly proportional to the product of the force of the pendulum weight and the distance of the horizontal offset of the gravity from the centroid. This distance is a function of the angle by which the pendulum is elevated. Higher elevations correspond to greater horizontal distance and, consequently, a higher torque.
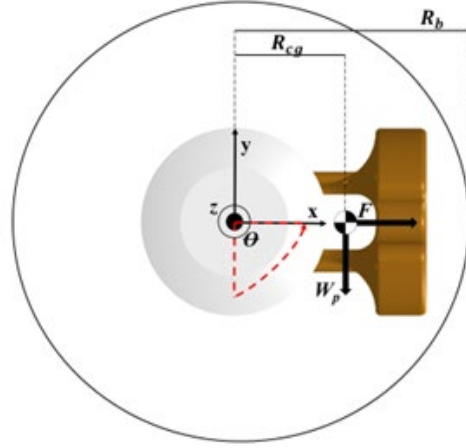
Figure 38 Free Body Diagram at equilibrium

The maximum propulsive force is when the pendulum is fully horizontal, and given by,

$$F = \frac{mgR_{cg}}{R_{ball}}$$

(3.1.1)

Where, m is total mass of the ball, g is gravitational acceleration, R_{ball} is Radius of the ball and R_{cg} is the Radius of center of gravity. Thus, the top speed of the ball is governed by either the equilibrium acquired when the propulsive force is countered by saturation of the actuator, or aerodynamic drag, whichever occurs first.

Robots need to climb slopes. The maximum angle of slope the robot may traverse, with no starting momentum, is equivalent to,

$$\theta = arcsin(\frac{R_{cg}}{R_{ball}})$$

(3.1.2)

Robots also need to climb steps or obstacles. The maximum step height the ball may climb, with no starting momentum can be found by,

$$h = R_{ball}(1 - cos(\theta))$$

(3.1.3)

34

Thus, the critical design parameter for maximizing hill and step climbing is the radius fraction of the center of gravity of the pendulum, with respect to the total radius of the ball. It is important to note that the top speed of the robot only improves with this radial ratio so long as the limiting factor of propulsion is the aerodynamic drag. Under conditions where the propulsion is, instead, governed by actuator saturation, moving the center of gravity outwards will only decrease the top speed. Maximizing this radial ratio also improves step climbing and slope climbing, even where aerodynamic drag is zero, like in the vacuum conditions found on the Moon.

Physical Layout

The Physical Layout of this system can be divided into 3 main categories namely, pipe assembly, pitch assembly and roll assembly. These three assemblies house the subsystems of the robot, which are, power, pneumatics, control and communication, locomotion, and the elastic shell.

The pipe assembly consist of (a) shaft, (b) end plates, (c) hubcaps, (d) clamping rings, (e) 56 teeth spur gears, (f) ball bearings, (g) spacers and (h) the elastic shell attached to the hubcaps. All the components (except elastic shell) are illustrated in the figure 39.
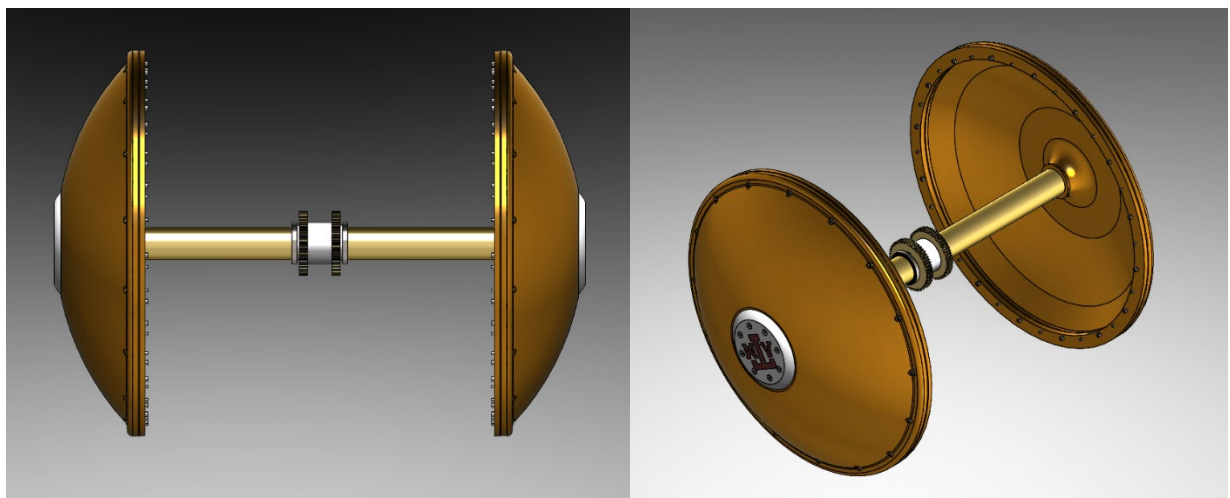
Figure 39 Pipe Assembly

The pitch assembly consist of (a) pitch housing, (b) neo motors, (c) bearings, (d) 24 teeth spur gears, (e) spacers, (f) 4:1 gear box. All the Components are illustrated in the figure 40.
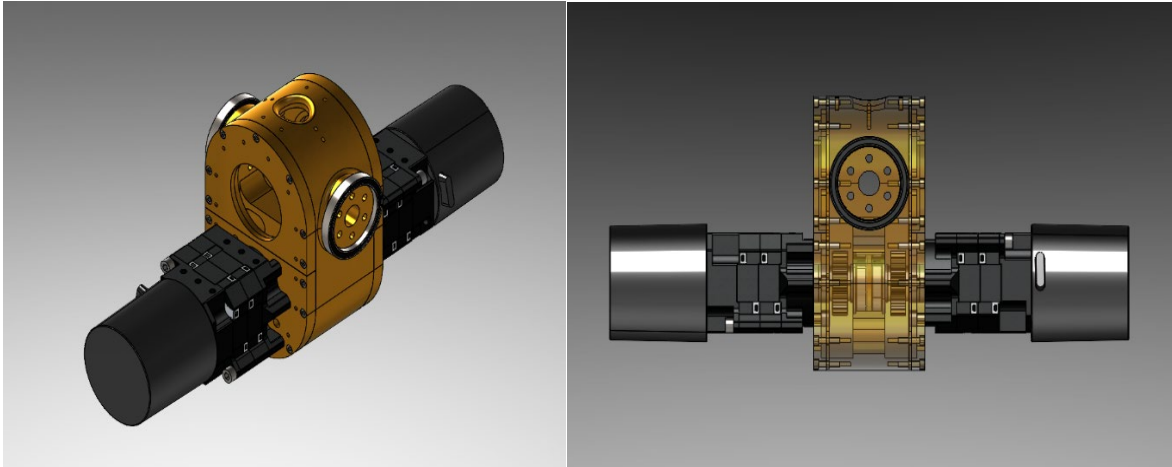
Figure 40 Pitch Assembly

The roll assembly serves as the mass of the pendulum, and houses major subsystems like power, pneumatics, steering locomotion, control, and communication. Each of these subsystems are discussed briefly in this chapter.
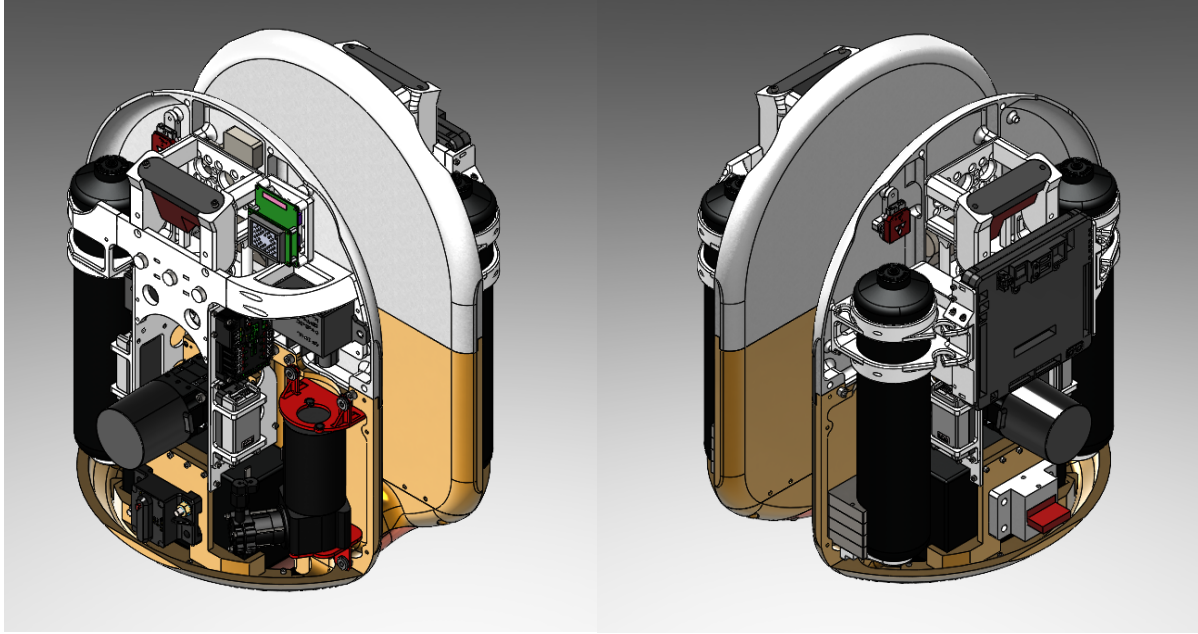
Figure 41 Roll Assembly

Power Subsystem

Two parallel-connected 12V, 7.2 Ah batteries serve as the power source for the robot. The batteries supply DC power to all the subsystems through series connection of a 120A braker and an e-stop actuated relay. The 120 A thermal circuit breaker protects the robot and other systems from drawing too much current.

Figure 42 120A Circuit Breaker
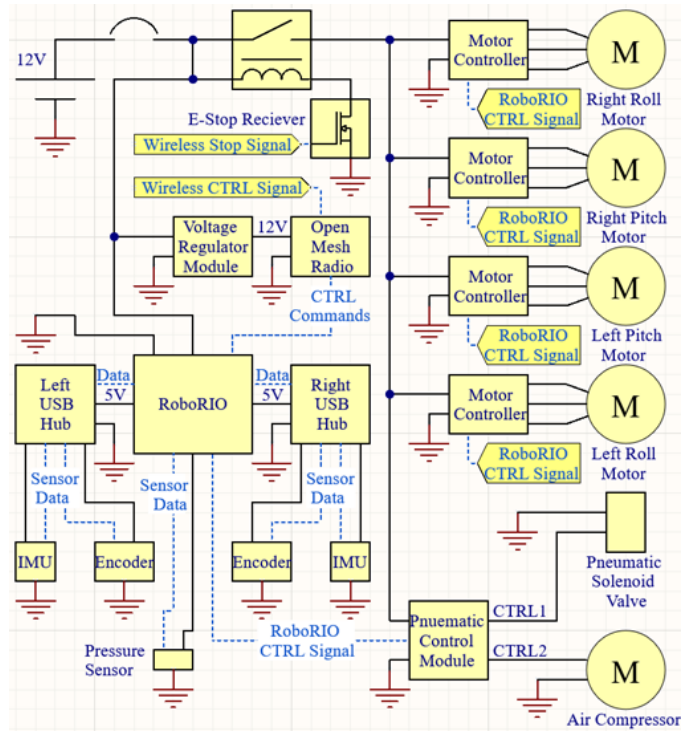
Figure 43 Detailed Electric layout
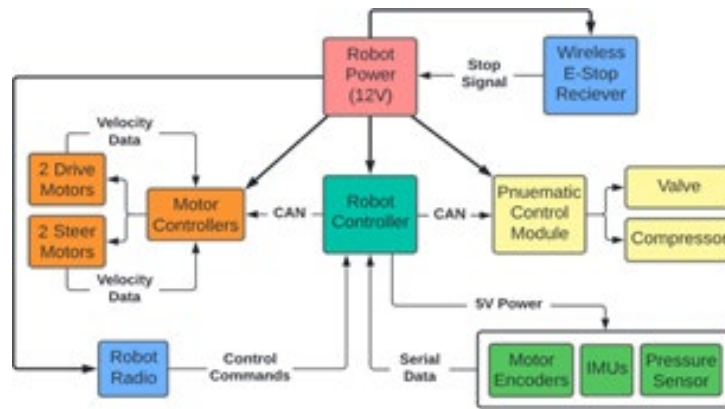
Figure 44 Simplified Electric Layout

Control and Communication Subsystem

The brain of the robot is the robot controller named roboRIO. It communicates wirelessly over radio, reporting serial data pulled from the sensors and to generate desired commands for the electric motor and pneumatics subsystems. Motor commands are sent to four drives with redundant steering and drive motors. A pneumatic control module (PCM) is used to command changes in the internal ball pressure. The PCM actuates the solenoid to vent the air from the tanks to the ball or operates the compressor to move air from the ball back into the tanks. The detailed pneumatic circuit is discussed in the later chapters.

Figure 45 Roborio 2.0

Figure 46 Radio

Locomotion Subsystem

The "Roboball" has two degrees of freedom controlled by 4 brushless DC Motors, namely 2 redundant pitch motors, and 2 redundant roll motors. The pitch motors drive the forward rolling while the roll motors steer the rolling in an arc. Should the pendulum be lifted by the pitch motors the torque is transferred to the endplates causing the ball to roll in the forward motion. Similarly, should the roll motors lift the pendulum the torques is again transmitted to the endplates causing the ball to steer the rolling axis. Figure 47 and figure 48 illustrates the forward rolling and steering conditions.
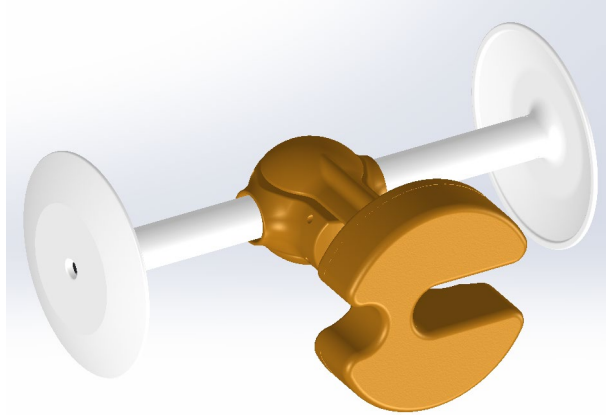
Figure 47 Forward Rolling
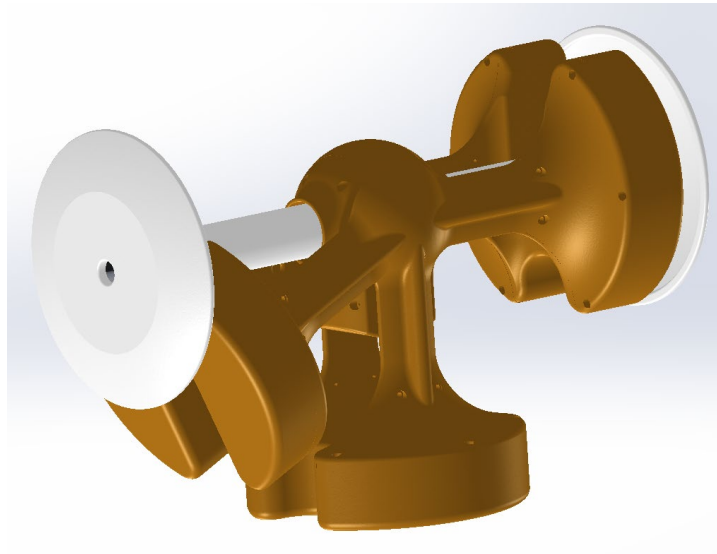
Figure 48 Different Steering Positions

The drive and steering actuators are Neo brushless motors running on nominal 12 V and have a free speed of 5676 rpm. It is a compact design with inbuilt 3-phase hall effect sensors for commutation and control, and a motor temperature sensor. then Neo provides better power to weight ratio than brushed DC motors.

Figure 49 Neo Motor

The Neo motors are controlled through by Sparx Max controller developed to be integrated with theses motors. The Sparx Max includes options for USB, CAN and PWM control, and can drive both 12 V brushed and brushless DC motors. It has two smart control modes options with a closed loop controller and follower mode.

Figure 50 SPARX MAX Motor Controller

The Lamprey is a 12-bit absolute encoder specifically designed for steering operation. It was selected because it is an absolute angle sensor and has a large hollow bore which can be fitted for measuring angular output without being at the shaft end. It had 4 interface alternatives, namely, USB, a 4 pin PWM style header, a 4 pin Molex picoblade connector and a 10-pin IDC cable arranged in a 5x2 pattern. The 2x5 pin header and IDC cable allows the Lamprey to be connected directly into the SPARX Max Controller.
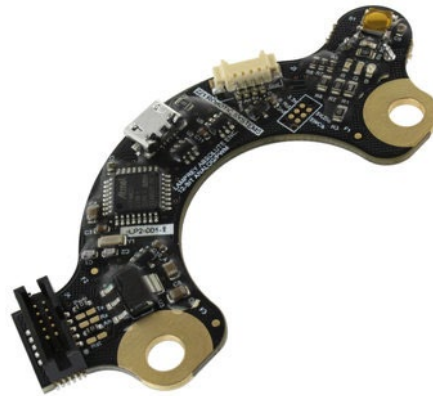
Figure 51 Lamprey absolute encoder

The VectorNav VN-100 is a miniature, high performance Inertial Measurement Unit (IMU) and Attitude Heading Reference System (AHRS). This IMU is a combination of gyros, 3-axis accelerometers, and magnetometers. It also has a barometric pressure sensor, a 32-bit processor, 400 Hz navigation data rates, 800 Hz IMU data rates, calibrated data, and a real-time 3D attitude solution that is continuous over the complete 360 degrees of motion. It has a process engine for disturbance rejection, adaptive filtering, and dynamic filter tuning. All sensors are

43

individually calibrated for bias, scale factor, misalignment, and temperature over full operating rate.

Figure 52 Vectornav 100-N

Pneumatic Subsystem

The function of this subsystem is to change the internal pressure of the robot. It has a (a) compressor, (b) 3 air tanks, (c) a solenoid valve, (d) analog pressure sensors, (e) Pressure relief valve, (f) Pressure gauge, and a (g) pressure switch.
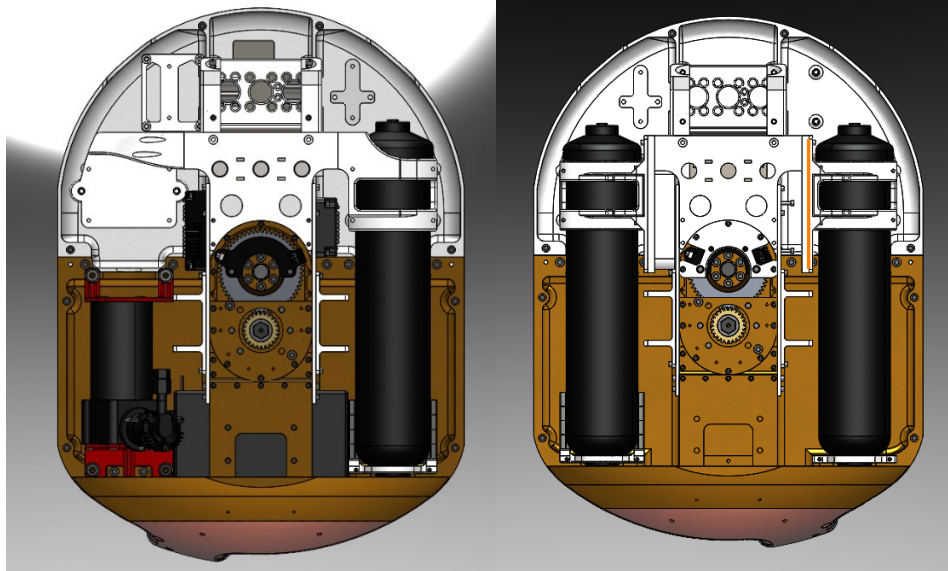
Figure 53 Pneumatic Subsystem

CHAPTER IV: ELASTIC BADDER AND RESTRAINING COVER

The novel factor of this robot is its elastic shell. The elastic shell comes with many advantages such as the ability to stow in a smaller volume, and variable pressure for driving on different terrain. Along with these advantages there are a few challenges to work with the elastic body such as the interface of the shell with the hubcaps, air-tight performance of that interface, optimizing minimum internal pressure, selecting the material of the shell, optimizing shell properties to give enough stiffness to maintain the pendulum off the ground and being tough enough to tolerate rough or dangerous terrain. These challenges and solutions are discussed in this chapter.

The motivation behind using two layers of elastic shell comes from the robot being able to operate at higher pressure than can be tolerated by an elastic ball. Naturally, anti -burst rubber is the first choice of material for the elastic shell. However, the elastic properties of this material will result in expansion and elongation of the rubber beyond the required dimension. The 2003 "RobBall" was only able to tolerate 0.1 PSI. Tomi J. Ylikorpi and et. developed a single shell ball with maximum pressure of 0.6 Psi. The second elastic layer or restraining layer, as the name suggests, acts as an exterior barrier to the rubber bladder allowing the robot to contain higher pressure with the acceptable dimensions. To test this hypothesis, a simplified test ball was developed with flat end plates and an emulator shaft to replicate the final robot dimensions.

We have discussed the design of the robot in chapter 3. There are 3 major concerns in designing and developing the skin of the robot. The first is the interface of the two elastic bodies, the second is the interface of the rings with the elastic body, and the third is the interface of the rings with the endplates. For simplification, a commercially available ball for horse exercise is

used as a restraining layer, designed to house a rubber bladder. The external shell is made of a relatively inelastic polyester material with thickness of 0.1 inch. Initially the shell and the bladder were sewed together, as shown in the figure 54 along with a rope to provide better gripping interface with the rings and the elastic body. The combined rope, ball and shell were fitted into groves in the clamping rings. The first-generation rings were developed taking into the consideration the dimensions of elastic body.

There are in total of 4 rings and 2 end plates. The elastic body is clamped between the two rings and the rings are attached to the endplates. Figure 55 shows the interfaces. In this design the rope will be completely gripped between the two rings and the outer edge with gripping extrusions on the ring to prevent the rope from slipping from the rings. This design did not show much promising results as air was leaking through the stitching between rubber bladder and the shell, as well as through the ring-elastic body-ring sandwich like structure. Moreover, as the screw holes are not exactly centered on the width of the ring, the clamping force of the screws was pinching the rope and was opening the outer edge, resulting in the rope being pulled from the rings.
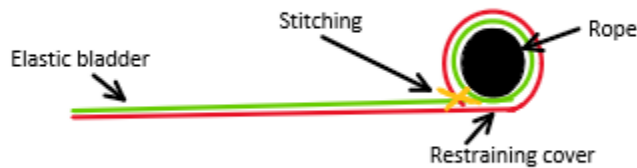
Figure 54 Bladder and Restraining Cover interface
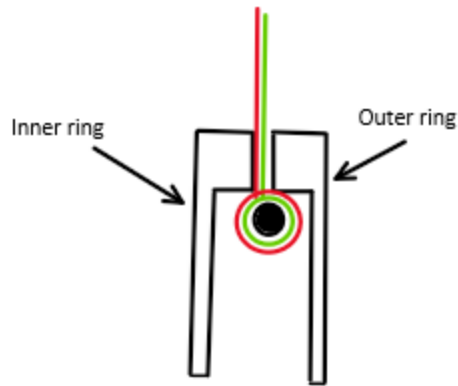
Figure 55 Cross sectional view of clamping the elastic bladder in first generation rings

The second-generation rings addressed the slipping of elastic body from the rings. Hence, the new rings capture the rope between two ridges on both ends of the rings. Only the inner ring is modified, the inner ring has an extrusion on both ends and the inner extrusion closes the gap between the two ring completely avoiding opening of the outer edges. The stitching style of the bladder and shell was changed with a stronger seem than before. This set-up allowed us to hold a pressure just above 1 psi before the ball tore at the interface with the shell. the conclusion was that putting holes in the rubber was doing more damage than good. Thus, a change in the interface between bladder and shell was needed. The next iteration tackled this by gripping the rubber bladder alone with two rings and the outer shell is over the end plates. The coefficient of friction is larger between the bladder and the aluminum rings than the previous polyester material and the aluminum rings, providing better grip.

With the existing first-generation rings, a test with the bladder-only approach gripped by the ring was carried out and a significant increase in the performance was observed. The ball was steady at around 2.5 PSI without any failure. The outer shell was also revised to be concentric to

the bladder and the end plates by adding a draw string on one end and closing of the other side completely. The figure illustrates the revisions.
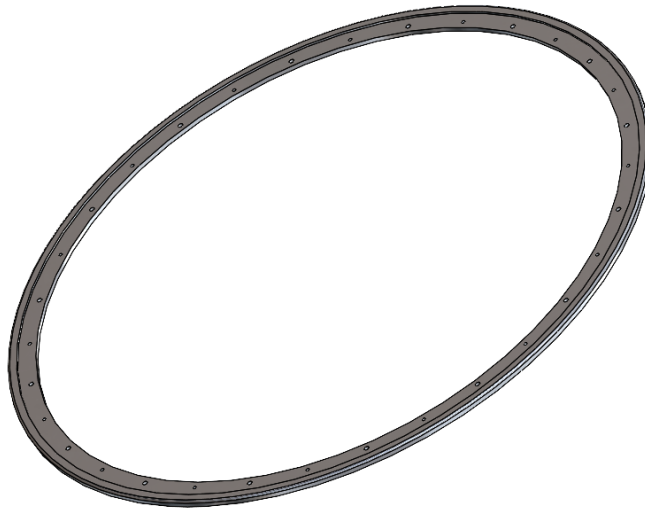
Figure 56 Generation 1 Ring Design

The above design eventually failed at 4 PSI due to the outer shell material failure. The previous modifications had made the ball stronger than the shell. Therefore, a custom-made shell was prepared with a new and stronger canvas polyester material. A significant number of minor adjustments in the design of shell were made along the way, before reaching the stable state where the ball was able to handle 3 to 3.5 PSI without failure. At this higher pressure, the failure was either the ball slipping out of the rings or the gore seams on the shell failing.

The third-generation rings were developed to solve the slipping problem, with an added ridge to grip the ball and more gripping range. The new rings were also made thicker axially, proving greater stiffness, less gaps between screws and more uniform clamping along the ring surface. The screw holes are upgraded to size 6-32 screws for greater clamping force, to assist the

tongue in the groove design for preventing the slipping of the rubber from the rings. The figure illustrates the new design.

Figure 57 Gen 3 Inner rings

Figure 58 Gen 3 Outer rings

The shell seams were also upgraded. The half-felled seams were replaced with a full-felled seam based on research of sail construction. The extra roll of the fabric prevented the fraying failure at

4 PSI. To accommodate the extra seam roll, the pattern had to be changed for manufacturing the shells.

Static Deflection Analysis

The ball is a hollow sphere of radius R_{ball} with wall thickness w and internal pressure P_i. While in contact with the ground (hard surface) the ball is compressed by some amount of y resulting in a circle of area $A(y)$ in contact with the ground. The figure illustrates the ball in contact with ground. From this the following geometrical relations can be concluded
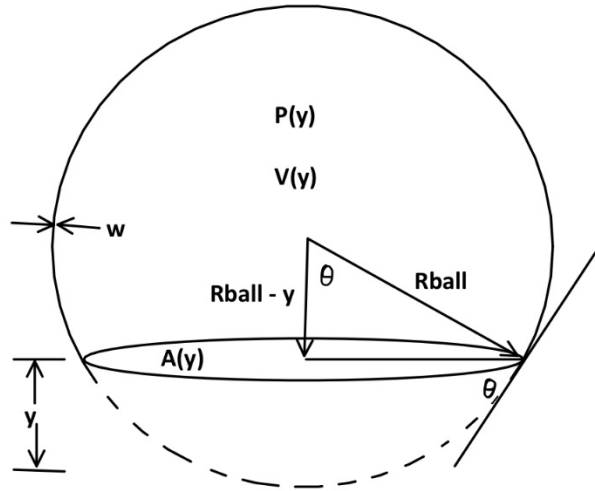
Figure 59 Geometry of a compressed ball

$$r(y) = \sqrt{\left[R_{ball}^2 - \left(R_{ball} - y \right)^2 \right]} \qquad (4.1.1)$$

$$A(y) = \pi \cdot \left[R_{ball}^2 - \left(R_{ball} - y \right)^2 \right] = \pi y (2R_{ball} - y) \qquad (4.1.2)$$

$$V(y) = \frac{4}{3}\pi R_{ball}^3 - \frac{1}{3}\pi y^2 (3R_{ball} - y) \qquad (4.1.3)$$

51

$$cos(\theta(y)) = \frac{R_{ball} - y}{R_{ball}} \qquad (4.1.4)$$

The compression of the ball will result in a pressure difference and subsequently will give rise to restoring force F_r. A restoring force F_s is a consequence of shear stain within the wall along the perimeter of the surface area in contact with the ground. Besides dissipative force is also generated during the compression and decompression. The dissipative force is much lower in magnitude with respect to the restoring forces and hence are neglected for the time being.

Restoring Force F_r can be formulated as follow,

Initially, pressure inside the ball is the gauge pressure $P_g = P_i - P_o$. As the ball compresses. The internal pressure changes due to volume compression from P_i to P_y, resulting in an upward restoring force,

$$F_r = [P_y - P_o] \cdot A(y) = [P_y - P_o] \cdot \pi y \cdot (2R_{ball} - y) \qquad (4.1.5)$$

For an isothermal compression of the gas,

$$P_y V(y) = P_i V(i) \qquad (4.1.6)$$

$$\Rightarrow P_y = \frac{P_i V(i)}{V(y)} = \frac{4R_{ball}^3}{4R_{ball}^3 - y^2(3R_{ball} - y)} \cdot P_i \qquad (4.1.7)$$

Thus,

$$F_r = \left[\frac{4R_{ball}^3}{4R_{ball}^3 - y^2(3R_{ball} - y)} \cdot P_i P_o \right] \cdot \pi y (2R_{ball} - y) \qquad (4.1.8)$$

52

$$F_r = 2\pi R_{ball}^2 P_g \left[\left(\frac{y}{R_{ball}} \right) - \frac{1}{2} \left(\frac{y}{R_{ball}} \right)^2 + \frac{3}{4} \left(1 + \frac{P_o}{P_g} \right) \left(\frac{y}{R_{ball}} \right)^3 + ... \right] \qquad (4.1.9)$$

Neglecting the second order and above higher order terms, we get,

$$F_r = 2\pi R_{ball} P_g y \qquad (4.1.10)$$

The above equation has the characteristics of Hook's Law. This is clearly accurate for small compression, $y \ll R_{ball}$. It is important to note where P_g is nearing zero, this model cannot be extended to gauge pressure being zero.

The restoring force F_s is calculated as,

$$\tau = \frac{F_s}{A_p} = \frac{F_s}{2\pi r w} = \frac{F_s}{2\pi \sqrt{\left[R_{ball}^2 - \left(R_{ball} - y \right)^2 \right]} w} \qquad (4.1.11)$$

The shear stress can be written in terms of shear modulus G and shear stain γ.,

$$\tau = \gamma G = \theta G = G \cos^{-1} \left(\frac{R_{ball} - y}{R_{ball}} \right) \qquad (4.1.12)$$

Hence,

$$F_s = 2\pi G w \sqrt{\left[R_{ball}^2 - \left(R_{ball} - y \right)^2 \right]} \cos^{-1} \left(\frac{R_{ball} - y}{R_{ball}} \right) = 4\pi G w R_{ball} \left[\left(\frac{y}{R_{ball}} \right) - \frac{1}{6} \left(\frac{y}{R_{ball}} \right)^2 - \frac{1}{30} \left(\frac{y}{R_{ball}} \right)^3 + ... \right]$$

$$(4.1.13)$$

Neglecting the second and higher order term,

$$F_s = 4\pi G w y \qquad (4.1.14)$$

Hence the total restoring force F_{total} is,

53

$$F_{total} = (2\pi R_{ball} P_g + 4\pi Gw)y = \alpha y \qquad (4.1.15)$$

The energy transformation during compression,

$$K_i = \frac{1}{2}\alpha y^2 - mgy + F_d y \qquad (4.1.16)$$

Where, K_i is the initial kinetic energy, which is equal to zero, and F_d is the dissipative energy which is also equal to zero.

Hence,

$$y = \frac{2mg}{\alpha} \qquad (4.1.17)$$

Analysis for the Robot

The above explained static deflection analysis is performed for the robot having the following parameters,

$$m = 45Kg$$

$$R_{ball} = 12inches$$

$$g = 9.81m/s^2$$

$$w = 0.1 to 0.5 inches$$

$$P_g = 1:15$$

$$G = 0.4Gpa$$

The hypothesis is that with increase in the thickness of the material the deflection, i.e., the compression of the ball in stationary position should reduce. Moreover, intuitively with increase

in pressure the compression should also reduce. This hypothesis is tested with the help of above analysis and MATLAB Simulation. The result obtained are as follows.

Figure 60 illustrates the variation of compression as pressure changes from 1 Psi to 15 Psi for different thickness of the material. It can be observed that the change in the compression is linear for all the thicknesses.
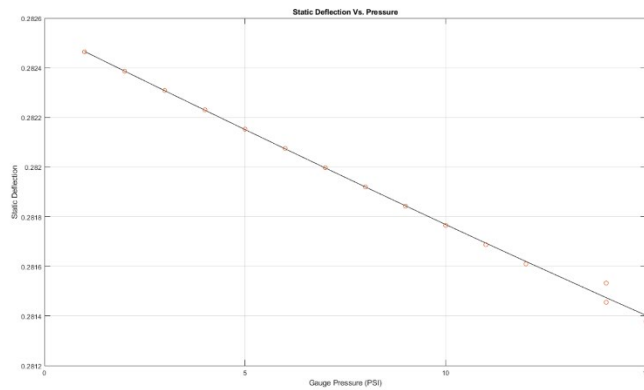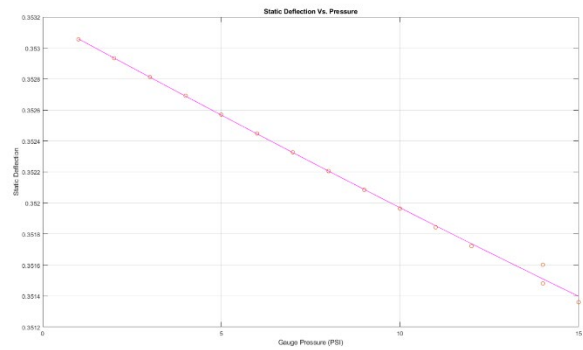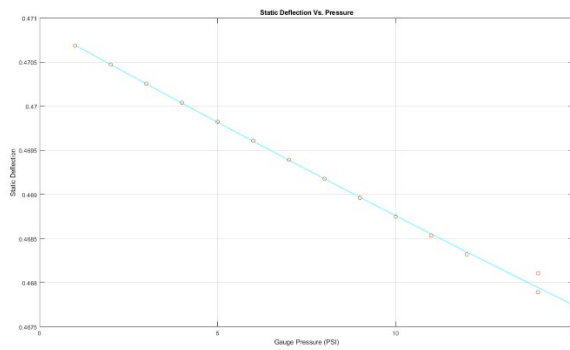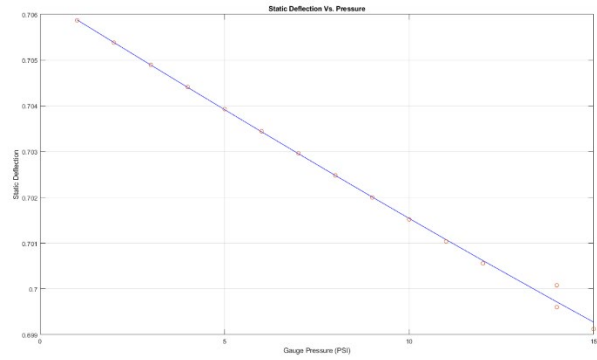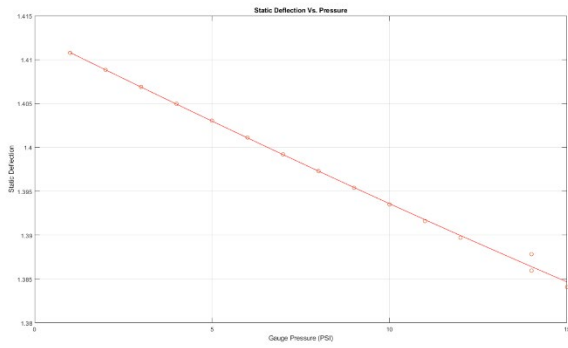
Figure 60 Variation in Compression with change in pressure (first row left) 0.1-inch thickness; (first row right) 0.2-inch thickness; (second row left) 0.3-inch thickness; (second row right) 0.4-inch thickness; (third row) 0.5-inch thickness
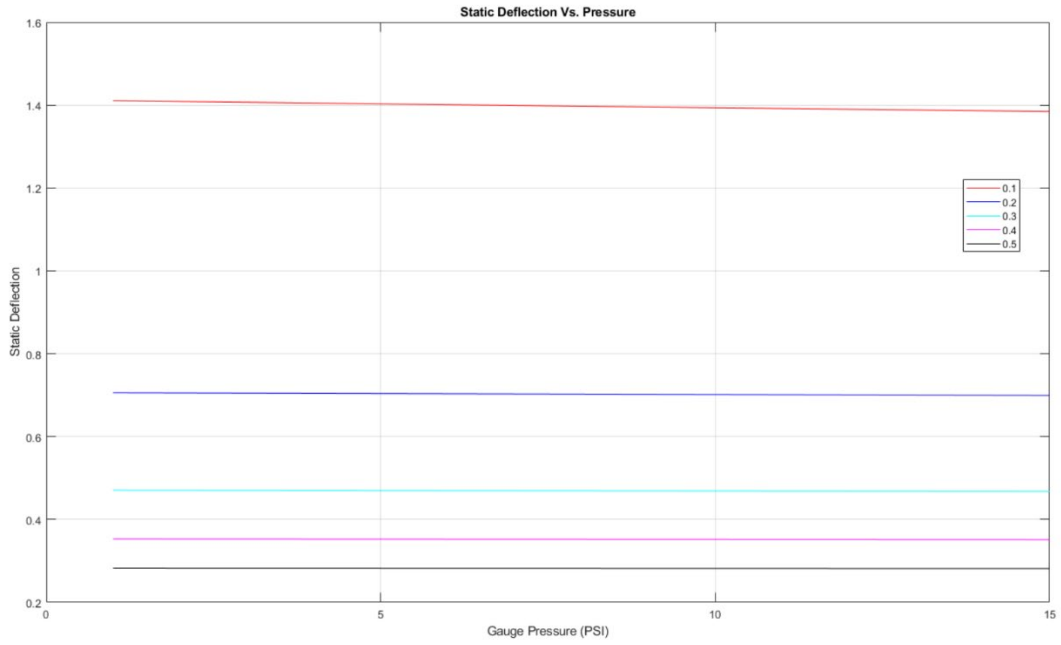
Figure 61 Variation of compression with change in pressure and thickness
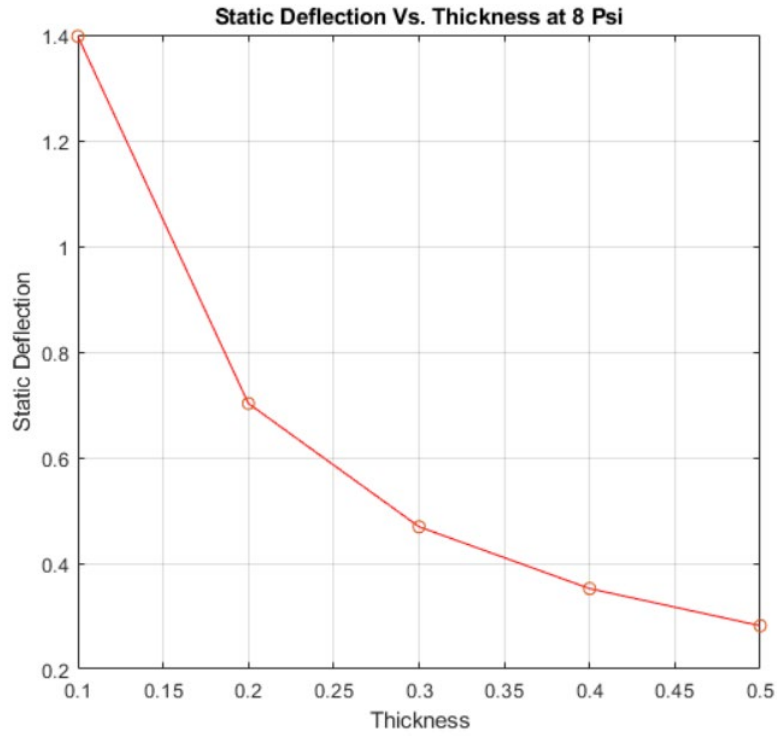
Figure 62 Change in compression with change in thickness

From figure 61 with increase in thickness the compression decreases. Figure 62 also illustrates the effect of change in thickness at a particular pressure of 8 Psi.

CHAPTER V: PNEUMATIC CIRCUIT

Automatic Tire Inflation Systems or ATIS's are quickly becoming popular in the automotive industry. For large trucks and trailers maintaining the correct pressure in all the tires is crucial for safety on the road, and improved performance off road on soft terrain. ATIS comes with a sensor, a battery, and air supply which automatically inflates the tires to desire values set by the user while moving. An equivalent system is proposed and implemented in the "RoboBall" for both adjusting to terrain needs as well as modifying the natural frequency and damping of the vertical bouncing mode of the robot. This chapter discusses the internal pneumatic circuit. The purpose of this subsystem is to automatically inflate and deflate the spherical ball with the user command.

Preliminaries

Before diving into the details on the robot subsystem few basic terminologies and concepts used throughout this chapter are summed up in this subsection.

Direction Control Valves:

Direction control valves or DCV, as name suggest are valves to control the flow of fluid. The functionality of the direction control valve is to allow or stop fluid flow or change the direction of the flow. A Direction control valve is a 2-way valve. A 2-way valve will allow the flow or stop the flow. A 3-way DCV are used for a single acting cylinder where one port is for the inlet, the second is for the flow to the actuator and the third is for the exhaust from the actuator. Some 3-way valves have a middle position where all the ports are blocked. Commercial 4-way valves have 2 position and 3 position options. A 4-way valve with 2-positions there are two positions can route fluid flow from port 1 to 4 or 2 to 3, in position 1. The second position routes flow from 1 to 2

and 4 to 3. Ports 1,2,3,4. A 4-way valve can be operated in 3rd position where there is no flow from any port. A 4-port valve is shown in the figure 65.
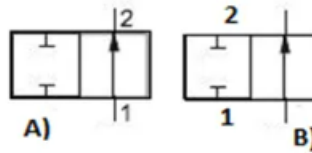
Figure 63 DCV 2/2
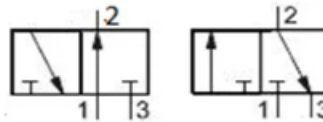
Figure 64 DCV 3/2
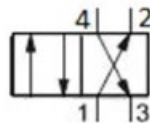
Figure 65 DCV 4/2

A 5-way valve is found most frequently in pneumatic circuits. A 5-way valve has the same function as a 4-way valve but with an extra exhaust port. Using two exhaust ports makes the valve smaller and less expensive. A 5-way is similar to a 4=way 3 position valve, but instead of the 3rd position being no fluid flow, the 5-way valve's 3rd position supplies flow from the inlet port to both the actuator ports.

These direction control valves are classified based on their operating method. They can be actuated manually, mechanically, hydraulically, and electrically. Manual operation uses a simple

leaver, or paddle actuator. Solenoids are the most common option for electrically actuated control valves.

Pressure relief valve:

A pressure relief valve is the safety measure used to avoid damage to a system due to over-pressurization. These are usually spring operated; the spring force is calibrated to relieve at the desired pressure.

Figure 66 Pressure Relief Valve

Pressure Switch:

A pressure switch is an electrically operated safety valve, where the compressor, control module and the pressure switch form a closed circuit. As soon as the calibrated pressure value is achieved the compressor is turned off. There is a lower limit where the compressor is turned on as well. The disadvantage of a pressure switch is it is not designed for releasing air out, instead just turning off the compressor. Should the pressure increase beyond the limit due to other reasons it will not be able to depressurize the system. Hence, a pressure relief valve and pressure switch are normally connected in series.

Figure 67 Pressure Switch

Check Valve:

A check Valve (also called a non-return valve, reflux valve, retention valve, foot valve, or a one-way valve) is a valve which allows the flow of fluid in only one direction. These are two port valves, with common styles being a ball check valve, diaphragm, stop, lift, swing, in-line, or reed. They are chosen corresponding to application. For a compressor or a pump, a back flowing high-pressure fluid will cause damage, thus a check valve is always desired in the forward direction. Table 1 illustrates the symbol of a check valve.

Pressure Sensor/ Pressure Transducer:

A pressure sensor or a pressure transducer is a device for pressure measurement of fluid inside a system. Pressure is expressed as the force required to stop the fluid from expanding, thus a senser generates a signal as a function of pressure applied acting as a transducer. There are different types of pressure sensors, such as absolute, gauge, vacuum, differential, sealed pressure sensor. They can be classified according to the force sensing technology, namely, Piezoelectric, capacitive, electromagnetic, optical and many more.

There are two pressure sensors used in this robot. Both are analog pressure sensors, one measuring the tank pressure and the other measuring the internal ball pressure.

Figure 68 Rev Analog Pressure Sensor

Figure 69 BMP 180Pressure Sensor
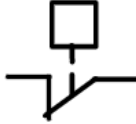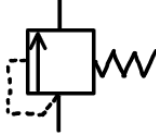
Tank / Reservoir:

A tank or a reservoir is a storage unit in the system. Table 1 enlists the symbol of a reservoir.

Figure 70 Clippard Air Tank/ Air Reservoir

Table 1 Pneumatic Component Name and Symbol

Component Name	Component Symbol
Pressure Tank	
Compressor	
Pressure Gauge	
Pressure Switch	
Pressure Relief valve	

Check Valve	
Flow regulator valve	
Directional Control Valve	
Pressure Sensor	
Manual valve	

Volume Calculations

An internal pneumatic system has been developed inside the ball to adjust and control the ball inflation. A key first step was to design the reservoir size in the tanks to achieve desired pressure change in the ball.

The volume of the spherical robot without internal assembly can be given by,

$$V_{ball} = \frac{4}{3} \cdot \pi R_{ball}^3 \tag{5.2.1}$$

Hence, $V_{ball} = 7238.23 in^3$

The internal components of the pendulum are incompressible and subtract from the variable pressure volume. Assuming the pendulum to be a cylindrical the volume is,

$$V_{pendulum} = \pi \cdot R_{pendulum}^2 \cdot h \qquad (5.2.2)$$

Hence, $V_{pendulum} = 1767.15 in^3$

To note, the volume of the main shaft is considered in the above calculation for the incompressible internal volume, beyond the simple cylinder.

Thus, the total volume of air inside the ball at atmospheric pressure is,

$$V_{air} = V_{ball} - V_{pendulum} \qquad (5.2.3)$$

Thus, $V_{air} = 5471.08 in^3$

From the data above we can calculate the number of reservoirs required to see the pressure change of 2.5 psi.

The standard available pressure reservoir which satisfies all the other design parameters is the Clippard 574 ml air reservoir.

Let's, define, $V_{tank} = 35.03 in^3$

Boyle's law states,

$$P_1 \cdot V_1 = P_2 \cdot V_2 \qquad (5.2.4)$$

Applying Boyle's law between the initial ball pressure and inflated, final ball pressure

$$P_{fball} V_{total} = P_{iball} V_{itotal} \qquad (5.2.5)$$

$$\Rightarrow 7.5 \cdot 5471.08 = 5 \cdot V_{itotal}$$

$$\Rightarrow V_{itotal} = 8206.62 in^3$$

The above V_{itotal} is the volume of the ball at 5 Psi. In other words, the difference between $V_{itotal} - V_{total}$ is the volume of air needed to be added to the ball at 5 Psi, to raise the pressure of the ball by 2.5 Psi.

66

Thus, $V_{additional} = V_{itotal} - V_{total}$ (5.2.6)

$$\Rightarrow V_{additional} = 2735.54 in^3$$

Applying Boyle's law once again,

$$5 \cdot V_{additional} = 120 \cdot V_{total-tank}$$ (5.2.7)

$$\Rightarrow V_{total-tank} = 113.98 in^3$$

The number of tanks required,

$$V_{total-tank} = n \cdot V_{tank}$$ (5.2.8)

$$\Rightarrow n = 3.25 \approx 3$$

Hence, 3 clipboard tanks filled with 120 Psi will increase the pressure of the ball by 2.3 Psi.

Pneumatic Circuit

This subchapter elaborates the design and working of the internal pneumatic system. The baseline and symbols of the components have been discussed in the first subchapter.
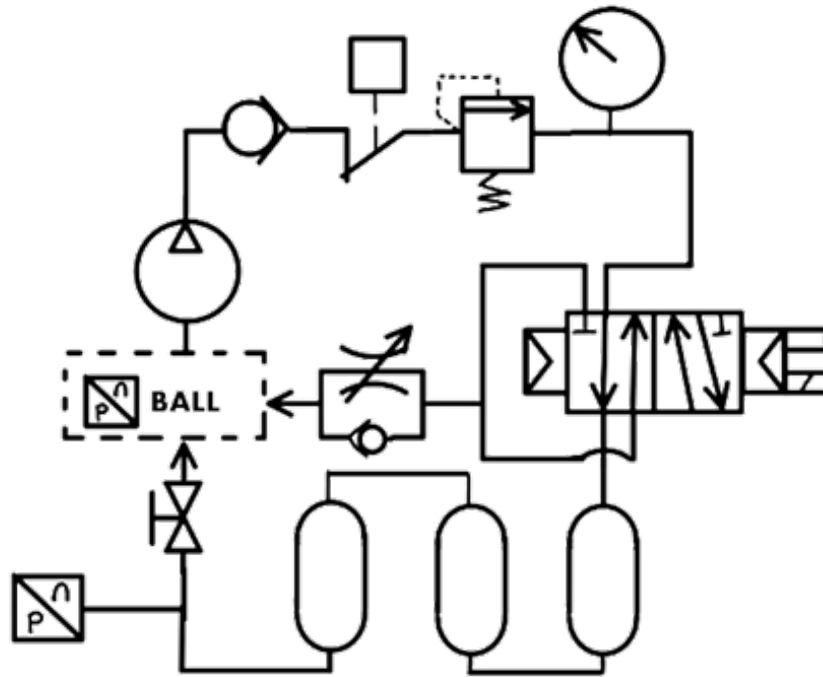
Figure 71 Pneumatic Circuit Layout

As seen in the above figure, the 3 pressure reservoirs are connected in series with each other and can totally hold 105.09 in^3 of air at 120 PSI. The 5 port, 2-way solenoid valve is connected in series with the check valve, pressure relief valve, pressure switch, and pressure gauge in between the compressor and the tanks. The outlet of the solenoid valve is directly open to the interior of the ball through a flow regulator to avoid a sudden pressure wave inside the ball while releasing the air. The two pressure sensors integrated with the system independently measure the tank pressure and the ball pressure. A check valve has been inserted after the compressor to avoid the damage to compressor due to back flow of the pressurized air. A manual valve is placed in the circuit to manually release the tank air to the atmosphere or the ball.

The pneumatic control module controls the compressor and the solenoid valve through the robo-Rio II microcontroller. The control module forms a closed circuit with the pressure switch and solenoid valve.

The pneumatic control module is the controller and controls 4 stages of pressure change. The first being the idle mode where no action is taken i.e., compressor and the solenoid valve both are non-operational. The second stage is constant ball pressure where the controller is reading data from the ball pressure sensor and act in accordance to keep the user-defined pressure of the ball. The third stage is where the tank pressure sensor is in command and tank pressure is maintained at any cost. Lastly, the user mode which allows the robot operator to decide when and which pressure sensor should drive the controller.

CHAPTER VI: DYNAMIC MODELING OF THE BOUNCING BALL

The behavior of the bouncing ball is a classic problem modeling energy before and after impact. The ball is modeled as spring-mass-damper system with three elemental properties, mass, linear stiffness, and viscous damping. The relation between these parameters described by M. Naguraka and S. Hung [5] is described in this chapter and then applied to the "RoboBall" which has a different size and elastic properties.

Preliminaries

Linear Stiffness k is described as a resistance to the external force trying to deform the elastic body.

Viscous damping c is a damping that is proportional to the velocity of the system.

Natural Frequency ω_n is the frequency at which a system oscillates when not subjected to a continuous or repeated external force.

Damped Frequency ω_d is the frequency at which a system oscillates when subjected to a continuous or repeated external force.

Damping Ratio ζ is a dimensionless measure describing how oscillations in a system decay after a disturbance.

Coefficient of Restitution e is a ratio of final velocity or the velocity after the bounce to initial velocity just before the impact.

Contact Time δT is time elapsed while the ball is in contact with the ground.

To study the behavior of the bouncing ball, consider an equivalent spring-mass-damper system as illustrated in figure 72. The ball is represented by its mass m, linear stiffness k and the viscous damping c.
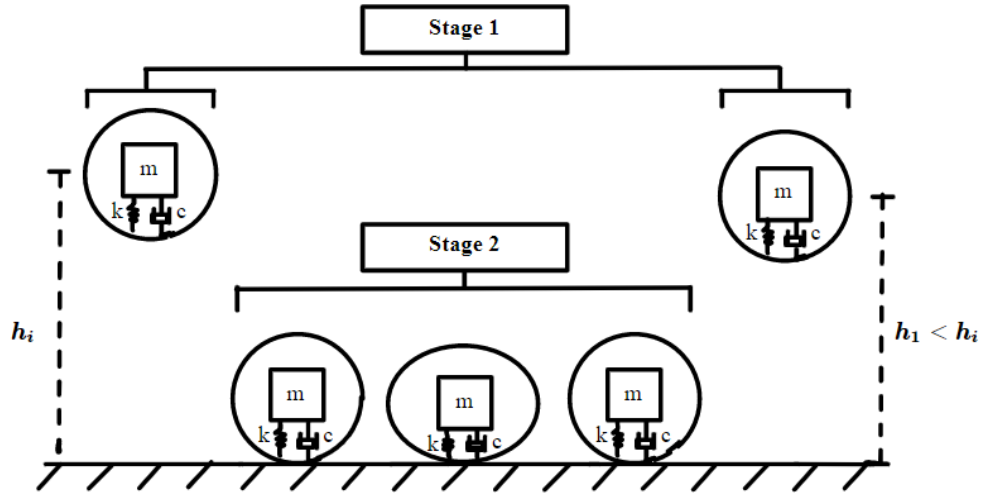
Figure 72 Spring-mass-damper model with different stages of impact at first bounce

The ball is modeled in 2 stages, first, when the ball is the air, and second, when the ball is in contact with ground. Assuming there is no aerodynamic drag the first stage can be modeled as,

$$m\ddot{x} = -mg \tag{6.1.1}$$

Where x is measured vertically up to the ball's center of mass. For ball released from rest height h_i, the initial conditions are $x(0) = h_i$, $\dot{x}(0) = 0$.

The second stage, when the ball is in contact with the ground, has the additional terms associated with the stiffness and damping of the ball. The equation of motion is as follows,

$$m\ddot{x} + c\dot{x} + kx = -mg \tag{6.1.2}$$

With initial conditions, $x(0) = 0$ and $\dot{x}(0) = -v_i$, where v_i is velocity of the ball prior to the contact with ground. Integrating the above equation gives,

$$x = \left[\frac{cg - 2kv_i}{2k\omega_d} sin(\omega_d t) + \frac{mg}{k} cos(\omega_d t) \right] \cdot exp\left(-\frac{c}{2m}t \right) - \frac{mg}{k} \qquad (6.1.3)$$

Where, ω_d is the natural damped frequency, which is given by,

$$\omega_d = \frac{1}{2m} \cdot \sqrt{4km - c^2} \qquad (6.1.4)$$

The equation (5.1.1) only represents the motion of the ball when in contact with the ground, i.e., $x <= 0$. The solution to the system needs to be underdamped, i.e., $\omega_d > 0$, for the bouncing behavior involving deformation, restitution and rebound. This also implies, $(4mk - c^2) > 0$.

For analyzing the bouncing the ball, the mass m is readily available whereas the parameters k, c or subsequently, the natural frequency ω_n and damping ratio ζ are unknown. The other unknown parameters, such as, δT, and coefficient of restitution, e, can be found experimentally. The parameters k and c can be determined mathematically, and can be determined by δT. and coefficient of restitution e is as follows,

$$e = \frac{|\dot{x}(\delta T)|}{|\dot{x}(0)|} \qquad (6.1.5)$$

$\dot{x}(0)$ is nothing but the initial velocity of the ball prior to the ground contact, i.e., v_i.

Rearranging equation (5.1.3) we get,

$$x = -\frac{v_i}{\omega_d} \cdot exp\left(-\frac{c}{2m}t \right) \cdot sin(\omega_d t) + \frac{mg}{k} \cdot \left[exp\left(-\frac{c}{2m}t \right) \cdot \left(cos(\omega_d t) + \frac{c}{2m\omega_d} \cdot sin(\omega_d t) \right) - 1 \right] \qquad (6.1.6)$$

Assuming $\frac{mg}{k} \ll 1$,

$$x = -\frac{v_i}{\omega_d} \cdot \exp\left(-\frac{c}{2m}t\right) \cdot sin(\omega_d t)$$ (6.1.7)

By setting the above equation to zero δT can be found as a non-zero minimum solution, which is,

$$\delta T = \frac{\pi}{\omega_d}$$ (6.1.8)

Differentiating the above equation and substituting $t = \delta T$, we get,

$$\dot{x}(\delta T) = \frac{cv_i}{2m\omega_d} \cdot \exp\left(-\frac{c}{2m}\delta T\right) \cdot sin(\omega_d \delta T) - v_i \exp\left(-\frac{c}{2m}\delta T\right) \cdot cos(\omega_d \delta T)$$ (6.1.9)

δT being very small, $sin(0) \approx 0$ and $cos(0) \approx 1$

$$\Rightarrow \dot{x}(\delta T) = v_i \cdot \left(-\frac{c\pi}{2m\omega_d}\right)$$ (6.1.10)

Hence, the coefficient of restitution is,

$$e = \exp\left(-\frac{c\pi}{2m\omega_d}\right)$$ (6.1.11)

By combining equations (5.1.8), (5.1.4), (5.1.11), the derived equation for k and c are following,

$$k = \frac{m}{\delta T^2} \cdot [\pi^2 + (\ln e)^2]$$ (6.1.12)

$$c = -\frac{2m}{\delta T} \cdot \ln e$$ (6.1.13)

Assuming k, c, and e are constant and independent of initial velocity v_i, δT will be constant.

The undamped natural frequency, ω_n, can be expressed as,

$$\omega_n = \sqrt{\frac{k}{m}}$$ (6.1.14)

73

$$\Rightarrow \omega_n = \frac{1}{\delta T} \cdot \sqrt{\pi^2 + (\ln e)^2} \qquad (6.1.15)$$

The damping ratio, ζ,

$$\zeta = \sqrt{1 - \frac{\omega_d^2}{\omega_n^2}} = \frac{c}{2\sqrt{km}} \qquad (6.1.16)$$

$$\Rightarrow \zeta = -\frac{\ln e}{\sqrt{\pi^2 + (\ln e)^2}} \qquad (6.1.17)$$

The above equation indicates that the damping ratio solely depends on the coefficient of restitution of the ball.

The total time and number of bounces can be found out experimentally. The total time elapsed is denoted as T_{total} and total number of bounces are n. Under the assumption δT and e are constants and there is no aerodynamic drag the following can be concluded.

For the kth bounce, height the ball can attain,

$$h_k = e^{2k} \cdot h_i \qquad (6.1.18)$$

Where h_i is the initial height from which the ball is dropped.

$$\text{As, } v_k = ev_{k-1} = e^k v_i = \sqrt{2gh_k} \qquad (6.1.19)$$

For the ball to attain equilibrium position,

$$h_n = e^{2n} h_i \leq \frac{mg}{k} \qquad (6.1.20)$$

Rearranging the equations δT in terms of e is as follow,

$$\delta T = e^n \sqrt{\frac{h_i}{g} [\pi^2 + (\ln e)^2]} \qquad (6.1.21)$$

74

The total time can be represented as the sum of total contact time and the time the ball is in the air. Hence,

$$T_{total} = T_{air} + T_{contact} \tag{6.1.22}$$

Where,

$$T_{contact} = n \cdot \delta T \tag{6.1.23}$$

And, assuming the contact time for all the bounces is constant,

$$T_{air} = \frac{1}{2}T_0 + \sum_{k=1}^{n} T_k \tag{6.1.24}$$

The Time in air for the kth bounce can be formulated as,

$$T_k = eT_{k-1} \qquad \forall k >= 2 \text{ and } T_1 = eT_0 \tag{6.1.25}$$

Thus,

$$T_{air} = \frac{1}{2}T_0 + T1 + \dots\dots + T_n$$

$$\Rightarrow T_{air} = \frac{1}{2}T_0 + T_1(1 + e + \dots + e^{n-1})$$

$$\Rightarrow T_{air} = \frac{1}{2}T_0 + T_0 e\left(\frac{1-e^{n-1}}{1-e}\right)$$

$$\Rightarrow T_{air} = T_0\left(\frac{1+e-2e^n}{1-e}\right) \tag{6.1.26}$$

Since,

$$T_0 = 2\sqrt{\frac{2h_i}{g}} \tag{6.1.27}$$

Thus,

75

$$T_{air} = \sqrt{\frac{2h_i}{g}} \cdot \left(\frac{1+e-2e^n}{1-e} \right) \tag{6.1.28}$$

$$\Rightarrow T_{total} = \sqrt{\frac{h_i}{g}} \cdot \left[\sqrt{2} \cdot \left(\frac{1+e-2e^n}{1-e} \right) + ne^n \cdot \left(\sqrt{\pi^2 + (\ln e)^2} \right) \right] \tag{6.1.29}$$

The above equation can be looked like an equation with single unknown, coefficient of restitution e, with regards to T_{total}, n, h_i all known parameters through experiment.

The contact parameters of coefficient of restitution, e and contact time δT can be found experimentally. To find theses parameters and establishing the relation between pressure and bouncing dynamics an experimental study was carried out. This chapter describes the methodology and experimental set up for gathering the bouncing test data.

Experimental Set Up

An equivalent ball was developed for this experiment. A ball with 2 flat end caps and a middle shaft to carry barbell weights representing the pendulum is illustrated in the figure 73. An in-house developed wireless pressure sensor is used to measure the internal pressure of the ball. The ball testbed emulates the final RoboBall in mass and uses the same ring/rubber/shell design previously described. It is essential to have the ball bouncing in the elastic region (not on the rings or hubcaps) to observe the pressure change and to avoid the damage to the rigid portion of the ball. Thus, the bouncing of the ball must be constrained in a way that maintains a vertical orientation while bouncing data is recorded. To tackle this challenge a test stand was designed and built as illustrated in the figure 74.
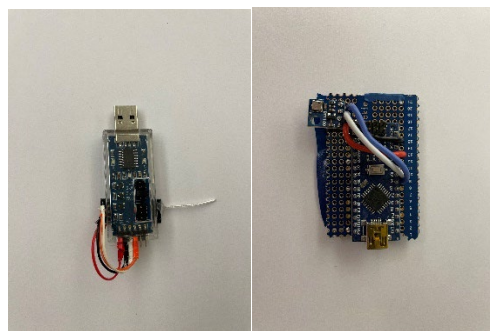
Figure 73 Wireless Pressure Sensor

Figure 74 Test stand for collecting Bouncing Data

As seen in the figure 74 two tension steel wires constrain the yaw and pitch motion of the ball as it rises and falls. The stand itself is restricting the translational motion of the ball in every direction other than the vertical.

Methodology

A ball is raised to a height of 0.4064 m and is dropped onto the laboratory floor. A Go-pro camera was installed to capture the bouncing of the ball at 240 frames per second. An internal pressure sensor, BM180 recorded pressure data at 44 Hz. The same procedure is followed for each iteration. A total of 5 tests were performed for each pressure. Starting from the low pressure of 2 Psi (gauge pressure) each set of 5 tests was conducted and then the pressure was increment 0.5 Psi, from 2.0 Psi to 5.5 Psi. Pressure was changed manually after each iteration.

Pressure Data

This subchapter presents the recorded experimental data. The graphs signify the internal pressure change for each bounce; hence the peak represents the highest compression and the rise and fall lines illustrate the contact with the ground. When the ball is in the air it is observed that the pressure decreases from the mean value, which signifies the change in the volume of the ball from the equilibrium position. Thus, the contact time is calculated from start of the rising hill line to the end of the falling hill line, while the time in air is time elapsed when the pressure falls below the mean value. The number of bounces is equal to the number of peaks recorded.

2 Psi Gauge Pressure
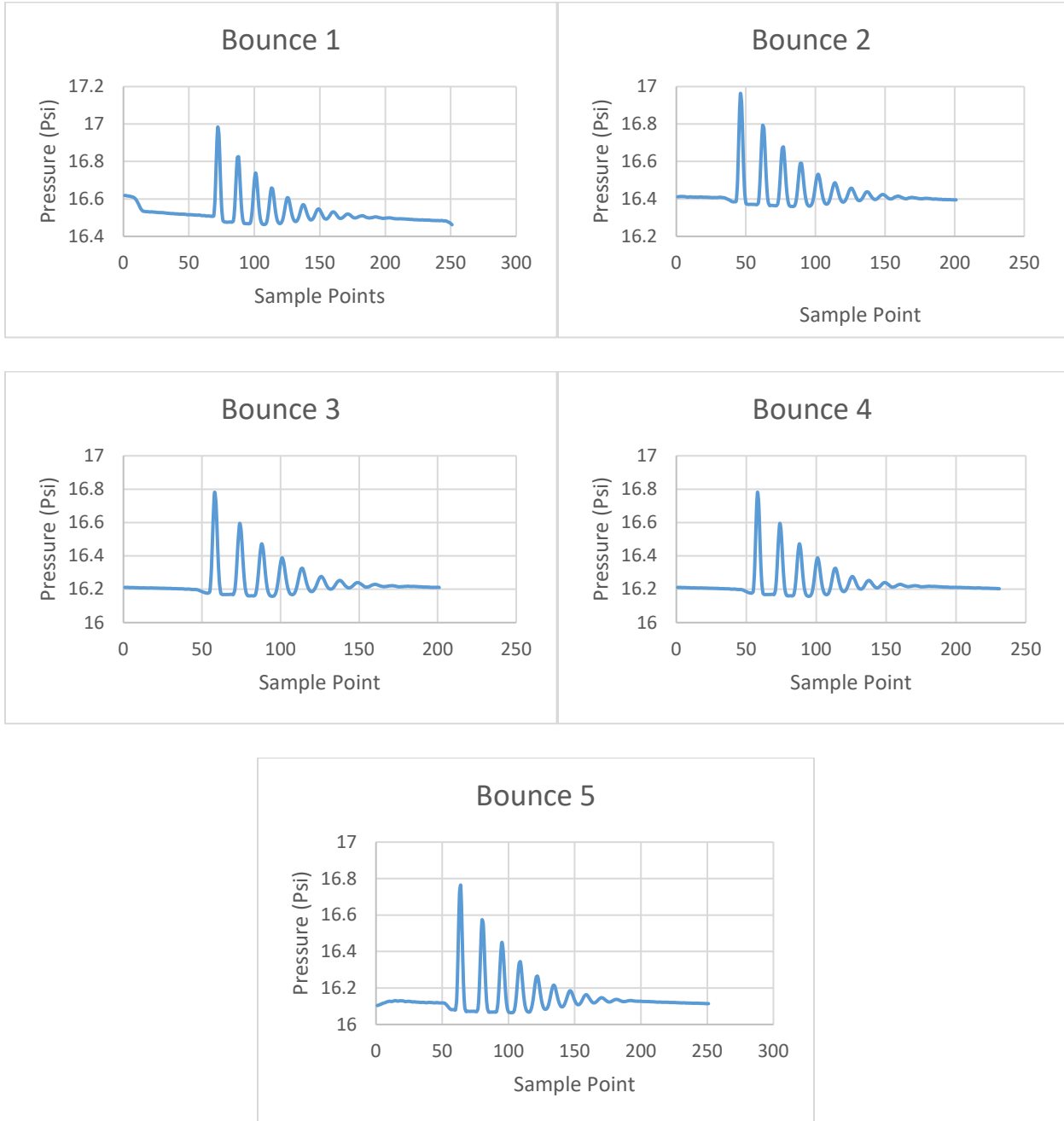
Figure 75 Pressure Data for bouncing of the ball at 2 Psi

2.5 Psi Gauge Pressure
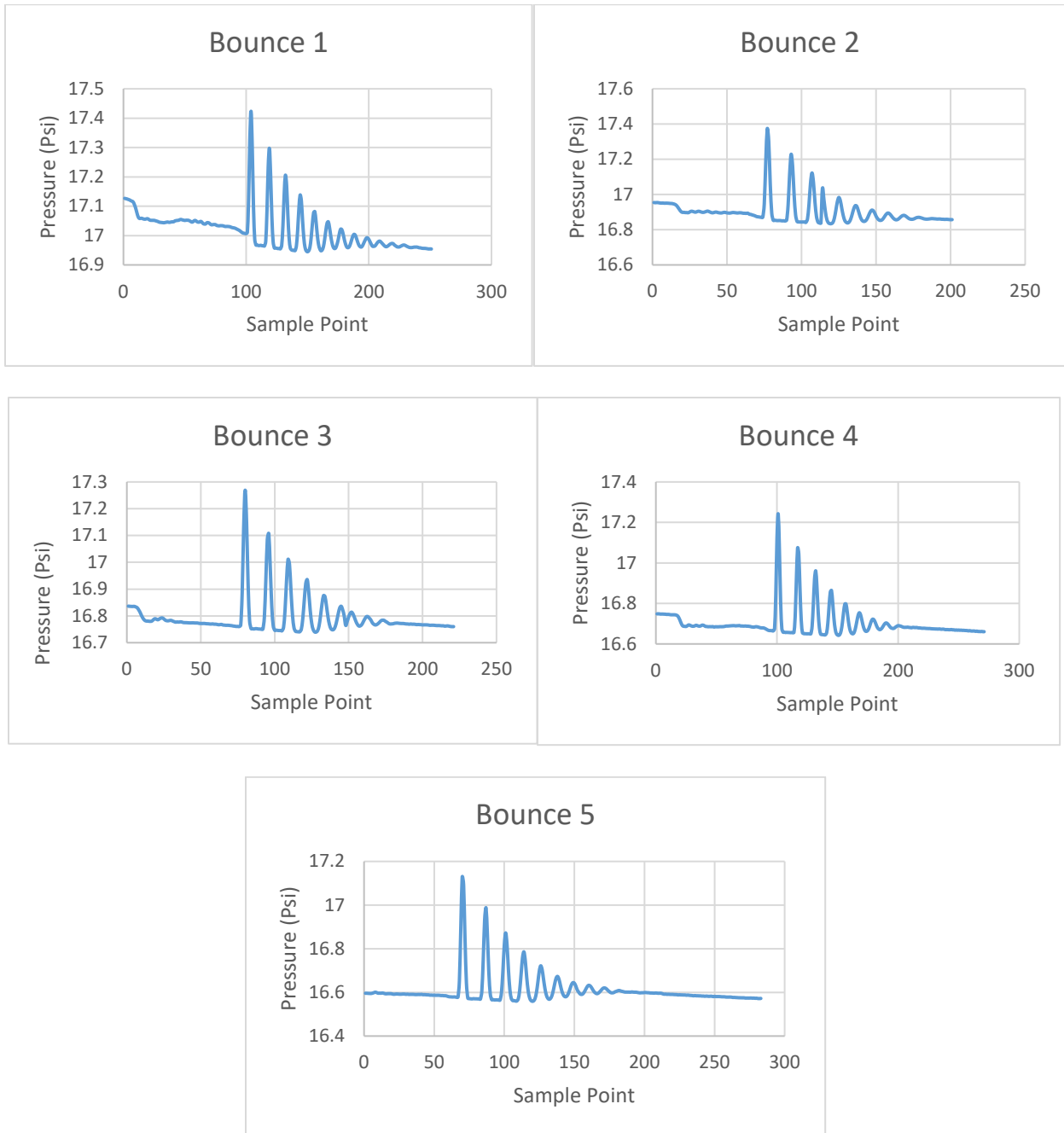
Figure 76 Pressure Data for Bouncing at 2.5 Psi

3 Psi Gauge Pressure
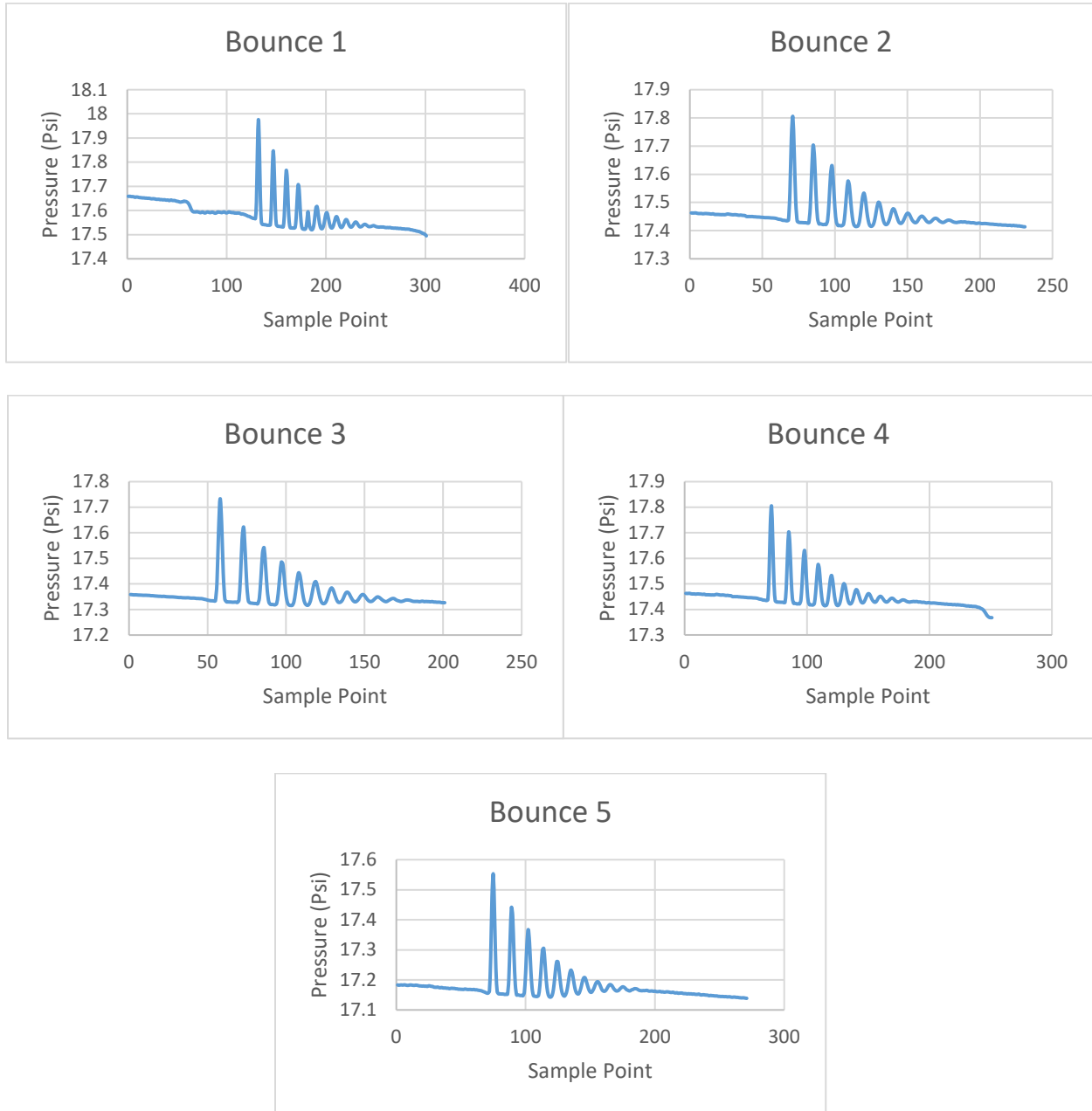
Figure 77 Pressure Data for Bouncing at 3 Psi

3.5 Psi Gauge Pressure
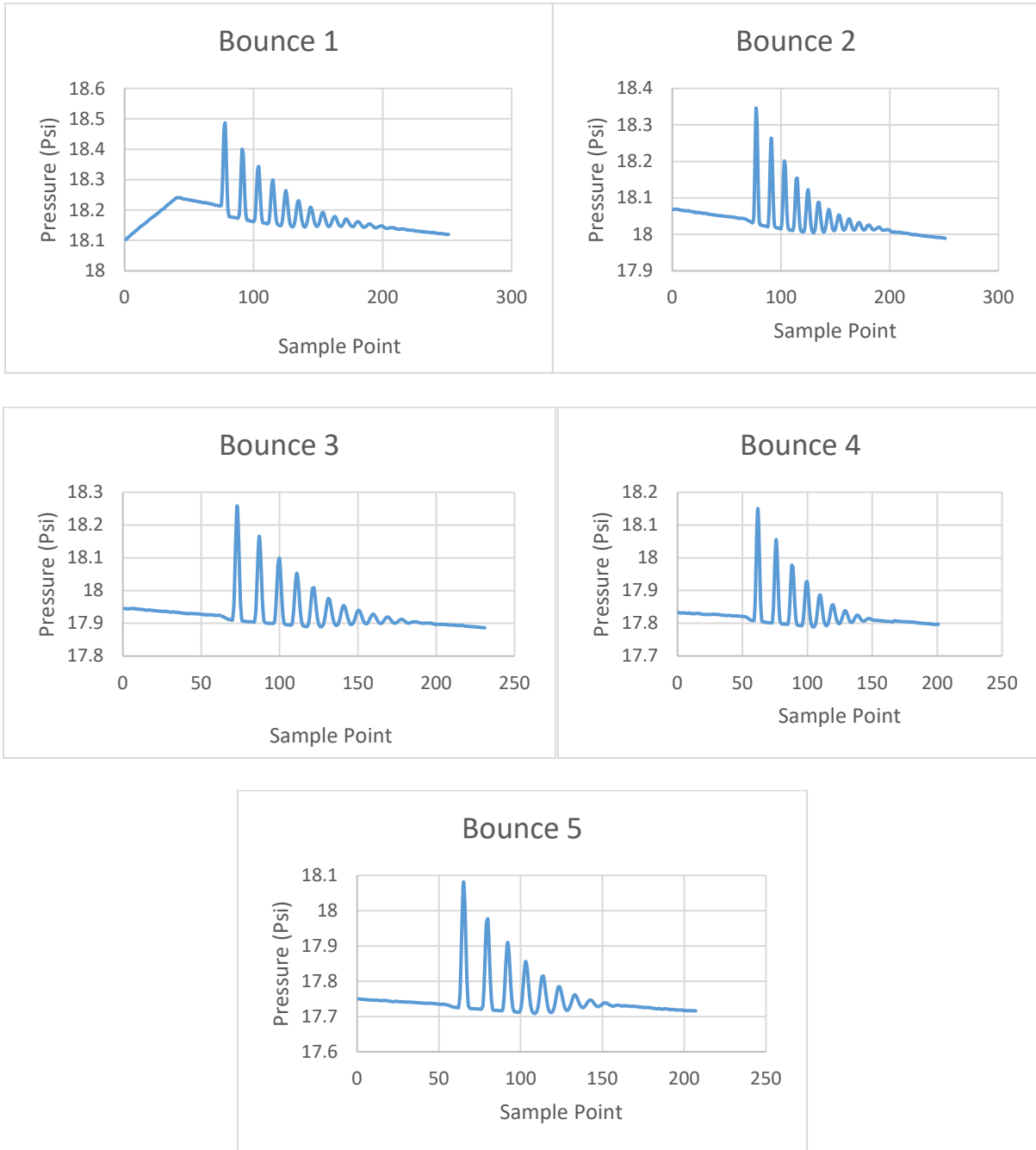
Figure 78 Pressure Data for Bouncing at 3.5 Psi

4 Psi Gauge Pressure
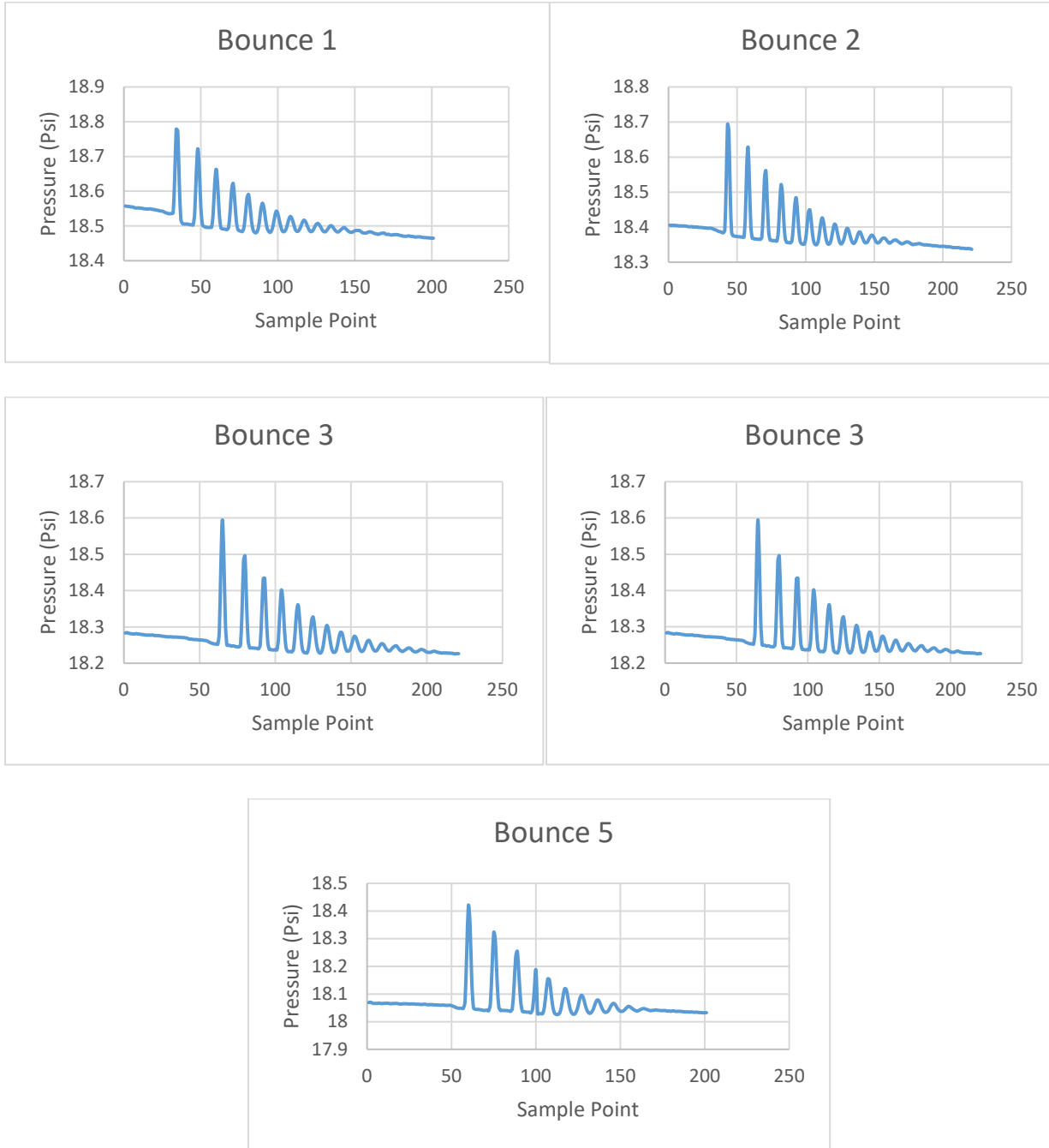
Figure 79 Pressure data for Bouncing at 4 Psi

4.5 Psi Gauge Pressure
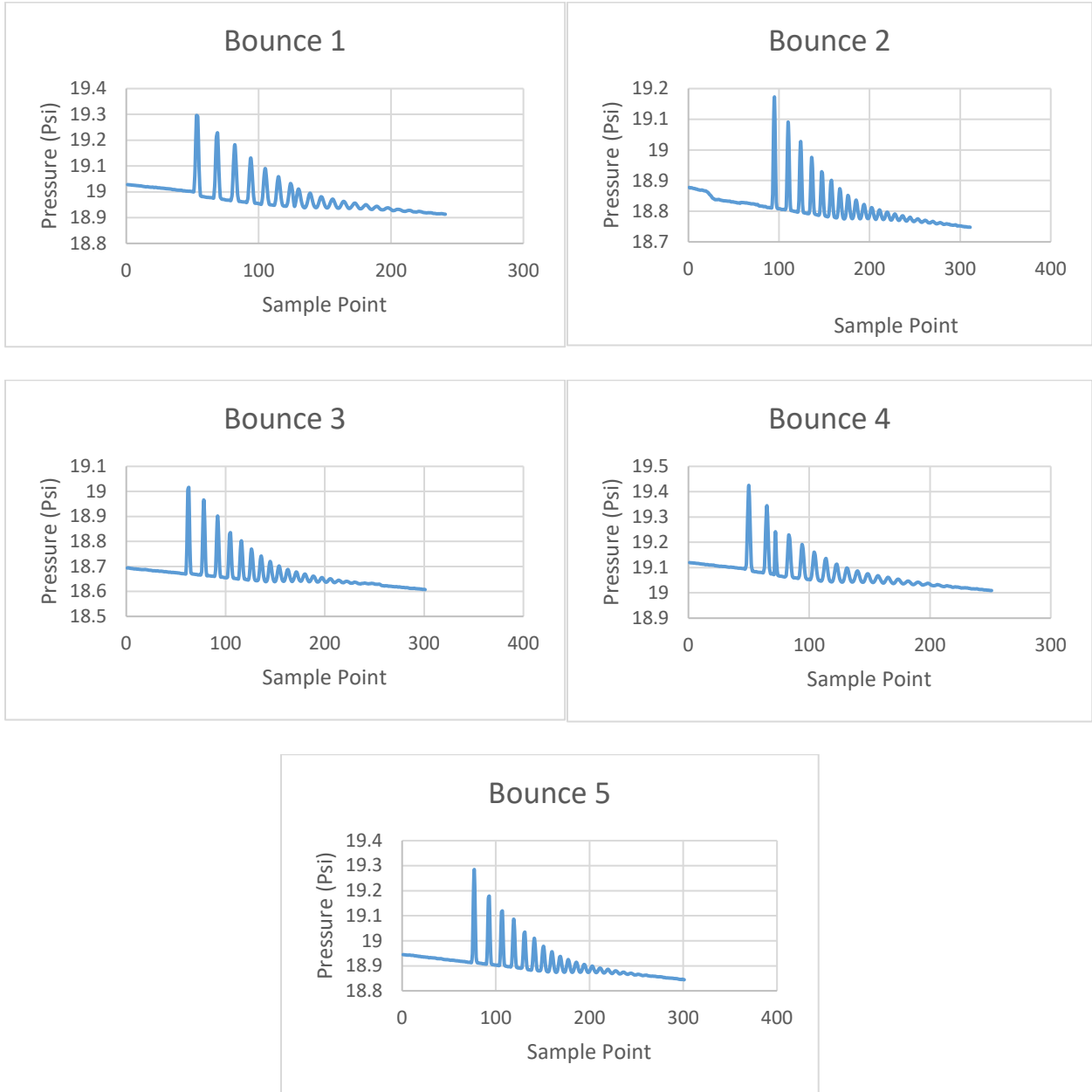
Figure 80 Pressure data for Bouncing at 4.5 Psi

5 Psi Gauge Pressure
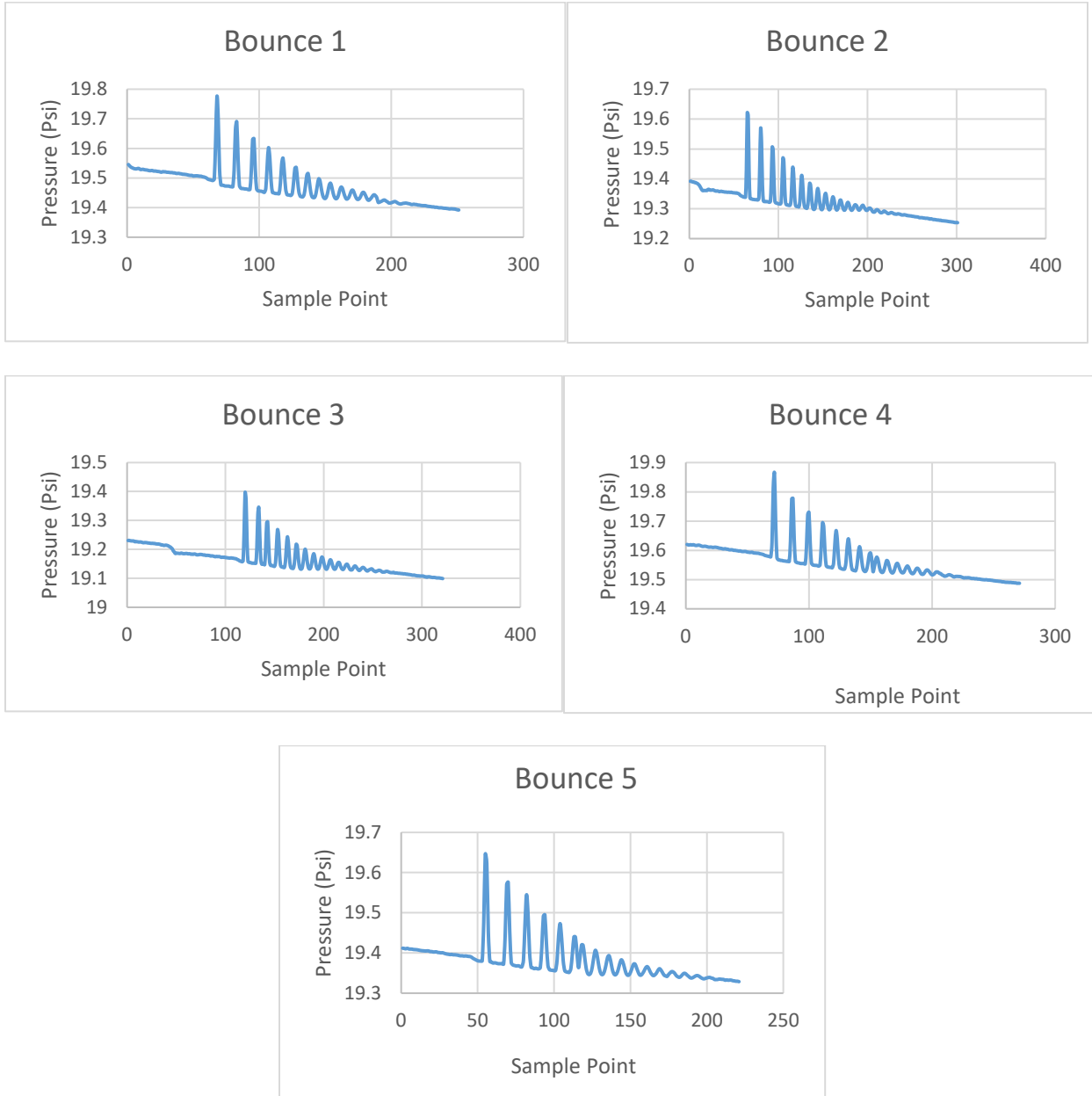
Figure 81 Pressure data for Bouncing at 5 Psi

5.5 Psi Gauge Pressure
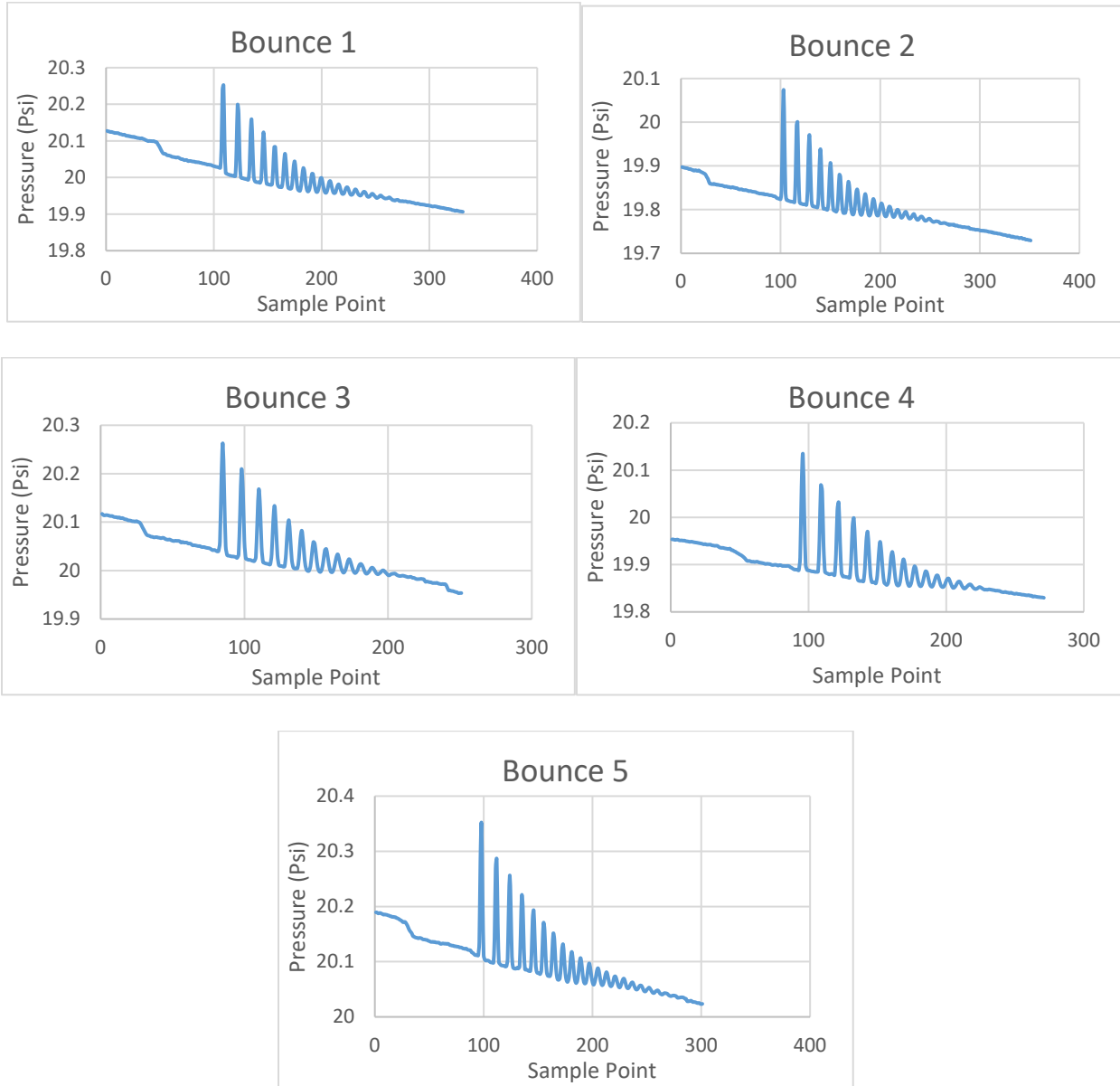
Figure 82 Pressure data for Bouncing at 5.5 Psi

Table 2 Experimental Data for Total Elapsed time and Number of Bounces

Pressure	Total time elapsed T_{total}	Number of bounces n
2	3.133	11
2.5	3.135	11
3	3.182	11
3.5	3.259	12
4	3.6	14
4.5	4.476	18
5	4.509	19
5.5	4.73	21

CHAPTER VIII: RESULTS AND CONCLUSION

Analysis from the Experimental Data

This chapter discusses the implementation of the dynamic model of the "RoboBall". Elapsed total bounce time T_{total} and number of bounces n have been found experimentally. From equation (5.1.29), coefficient of restitution e can be determined. With initial drop height being 0.4064 m, at 4 Psi, the total number of bounces was 14 and the total time elapsed was 3.6 sec. The coefficient of restitution is determined to be $e = 0.8334$ The figure 83 illustrates the change of coefficient of restitution with pressure. It can be clearly seen that with increase in pressure, the coefficient of restitution is increasing.
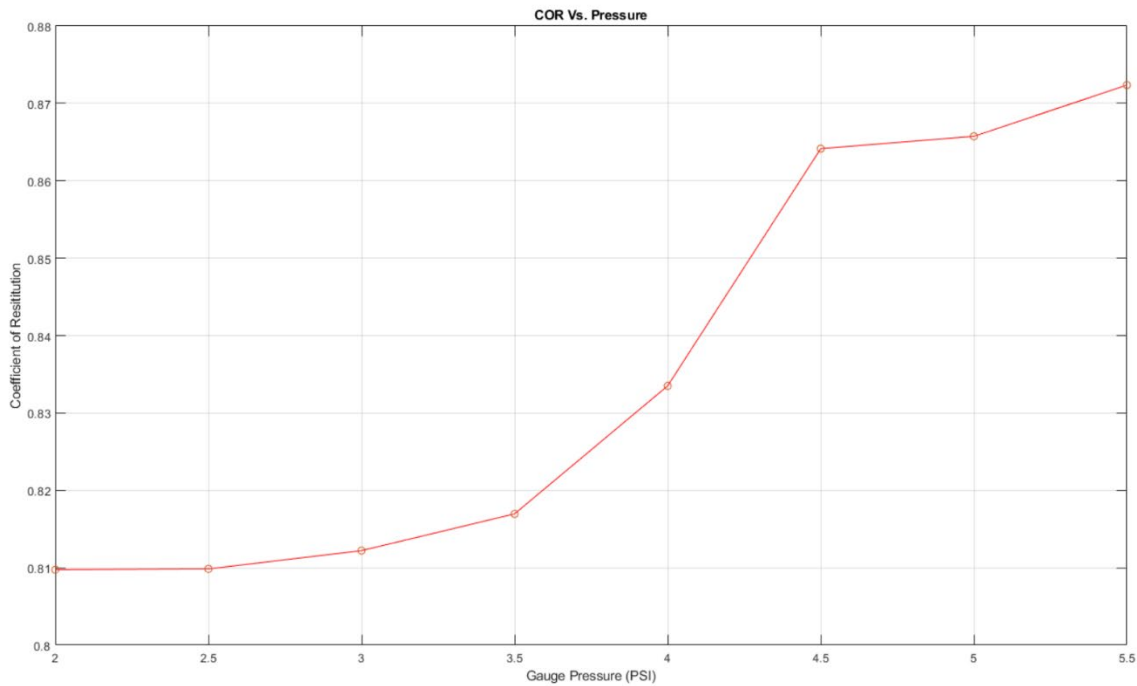
Figure 83 Coefficient of Restitution Vs. Pressure

89

Since, the coefficient of restitution, e is known, from equation (5.1.12), and equation (5.1.3) the linear stiffness, k, and Coefficient of damping, c can be calculated. The table 3 illustrates the obtained results.

Table 3 Changes in Linear Stiffness and Viscous Damping

Internal Gauge Pressure (Psi)	Linear Stiffness k (N/mm)	Viscous Damping c (N-mm/s)
2	102.31	0.2739
2.5	102.02	0.274
3	95.69	0.2611
3.5	126.11	0.2914
4	161.54	0.297
4.5	188.94	0.257
5	235.94	0.284
5.5	305.05	0.3064
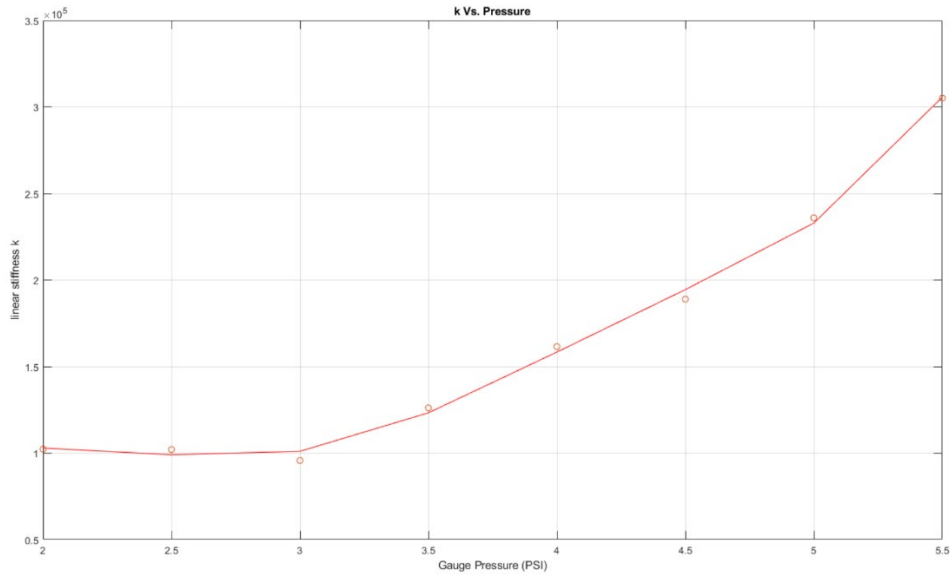
Figure 84 linear Stiffness Vs. Pressure

Clearly, from figure84 it can be observed that the linear stiffness grows in an exponential relation to internal ball gauge pressure. The damping ratio is shown to drop across the pressure range tested.

Values of the natural frequency ω_n, damping ratio ζ, and subsequently damping frequency ω_d, with the other known parameters such as e, c, k could be determined from equation (5.1.15), equation(5.1.17), and equation (5.1.4) respectively. The obtained results are listed down in the following table.

Table 4 Table of Natural Frequency, Damping Ratio and Damped Frequency corresponding to Pressure

Pressure (Psi)	Natural Frequency ω_n Hz	Damping Ratio ζ	Damping Frequency ω_d Hz
2	7.96	0.06702	7.94
2.5	7.95	0.06700	7.93
3	7.7	0.06670	7.68
3.5	8.84	0.06596	8.82
4	10.01	0.06374	9.99
4.5	10.82	0.05952	10.81
5	12.09	0.05633	12.08
5.5	13.75	0.05334	13.74
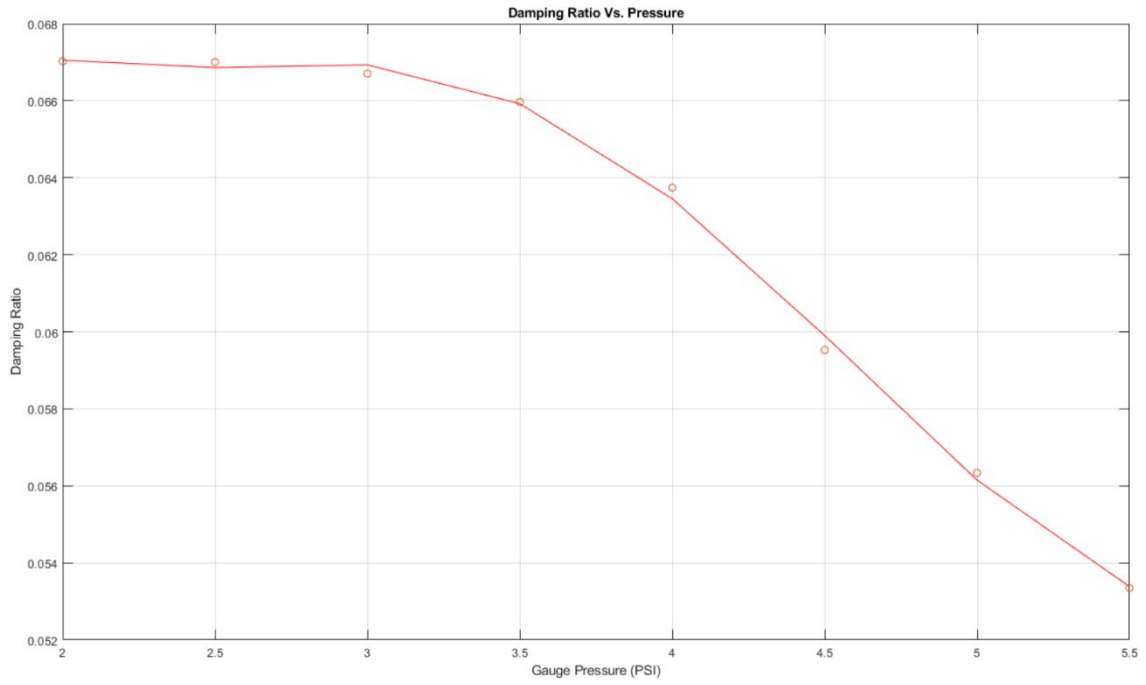
Figure 85 Damping Ratio Vs. Pressure
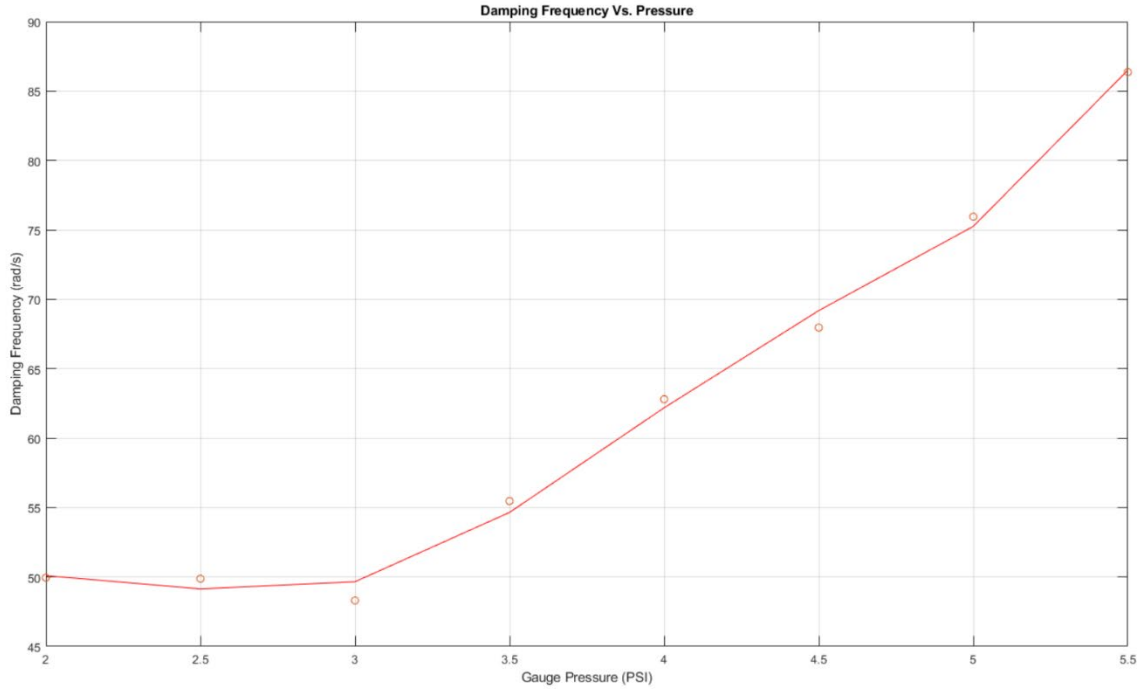
Figure 86 Damping Frequency Vs. Pressure

MATLAB Simulation

To verify the results obtained from the pressure data, a MATLAB simulation was built with the two stages of the ball bounce represented in a state space form. The resulting motion is plotted as a function of height with respect to time along with the variation of velocity. Referring to the chapter VI impact analysis, the equations (5.1.1) and equation (5.1.2) can be converted into state space form as follows,

Let's Define, $\dot{x} = x(1)$ and $x = x(2)$

Thus, equation for stage I, i.e., when the ball is in that air is,

$$m\,\dot{x}(1) = -mg \text{ and } \dot{x}(2) = x(1)$$

94

$$x\dot{(}1) = -g \text{ and } x\dot{(}2) = x(1) \tag{8.2.1}$$

The stage 2 equation of motion when the ball is contact with ground becomes,

$$x\dot{(}1) = -g - \frac{k \cdot pen}{m} - \frac{c \cdot x(1)}{m} \text{ and } x\dot{(}2) = x(1) \tag{8.2.2}$$

Where,

$$pen = (x(2) + R_{ball}) - h_i \tag{8.2.3}$$

Inputting the k and c values obtained from earlier subchapter the following results are obtained,
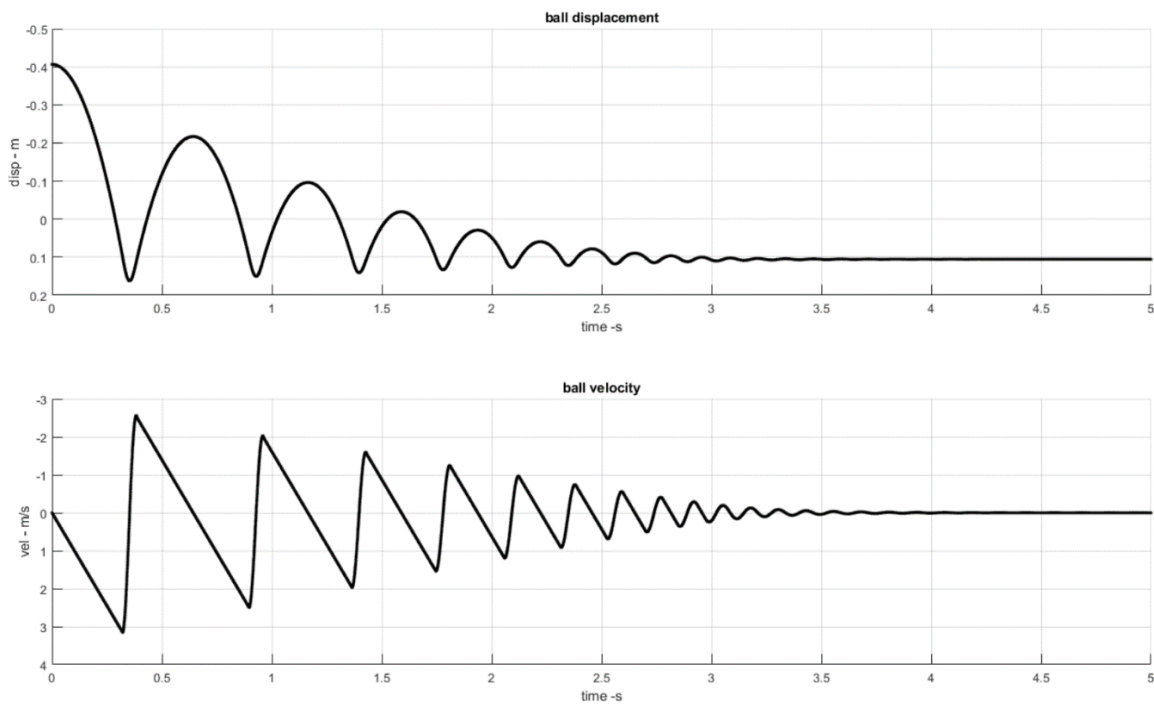
Figure 87 2 Psi Bouncing Simulation data

95
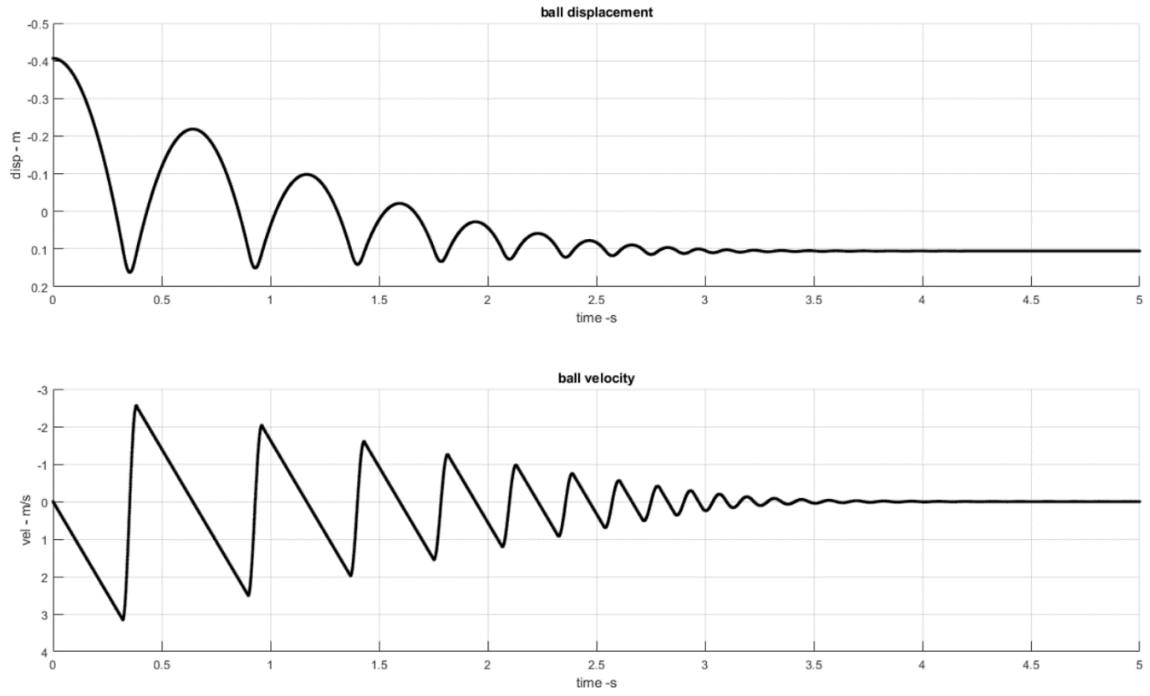
Figure 88 2.5 Psi Bouncing Simulation data
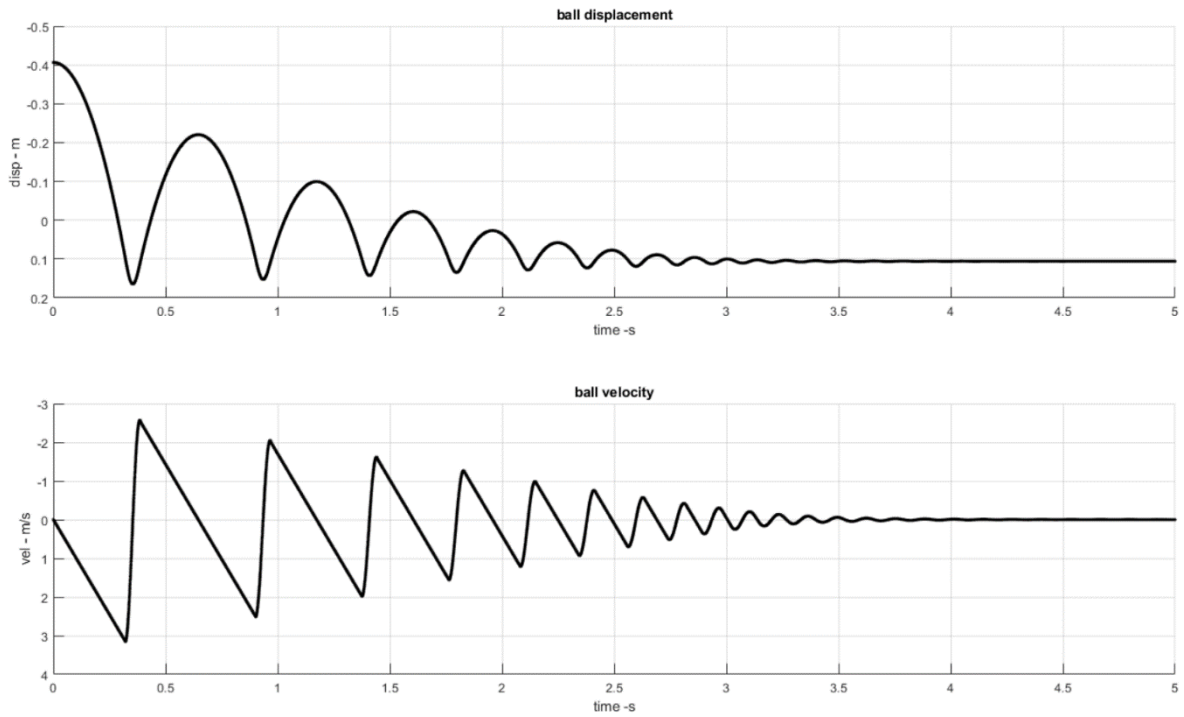
Figure 89 3 Psi Bouncing Simulation data
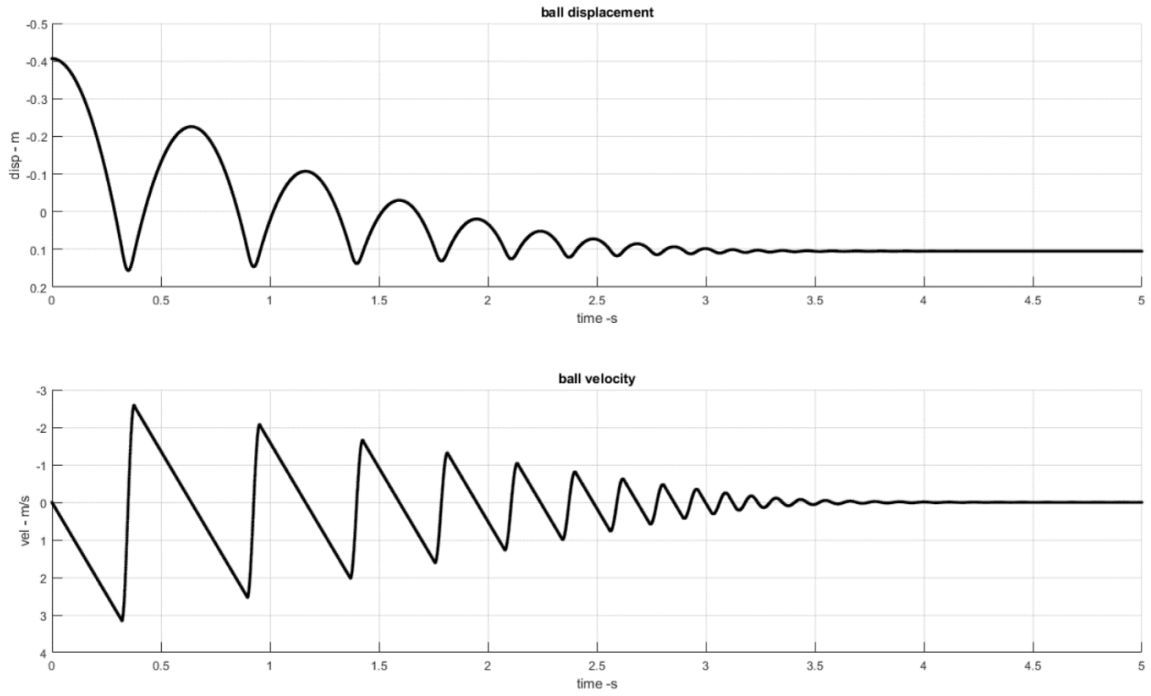
Figure 90 3.5 Psi Bouncing Simulation data
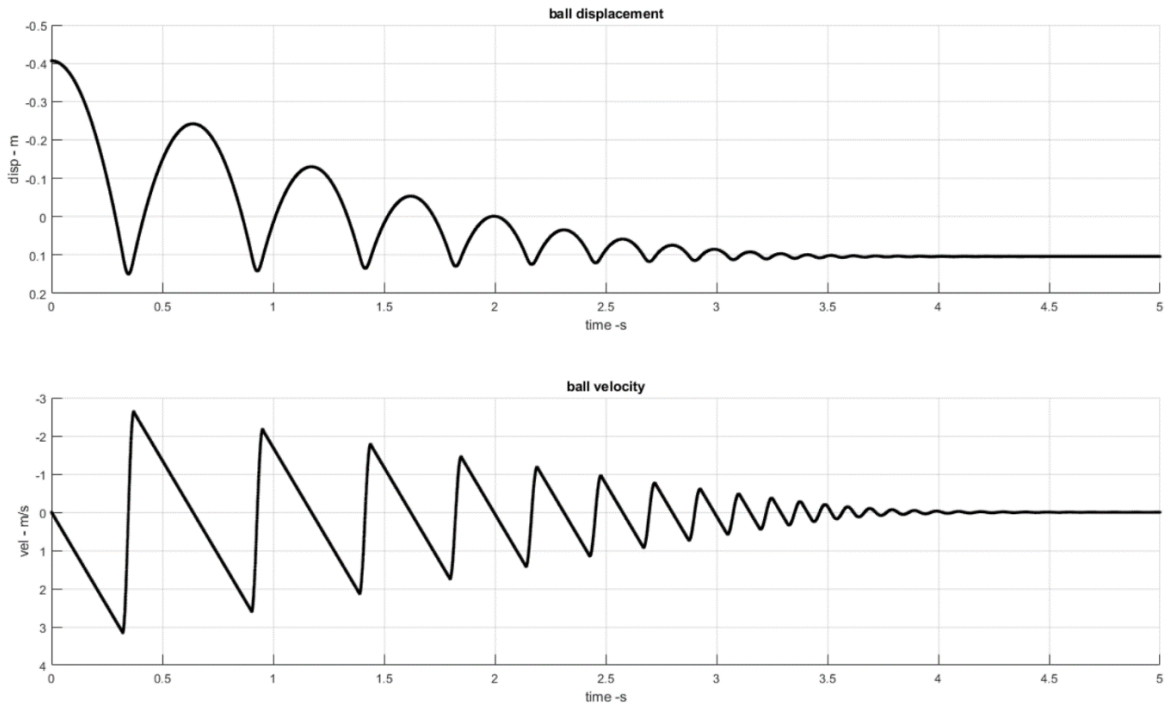
Figure 91 4 Psi Bouncing Simulation data
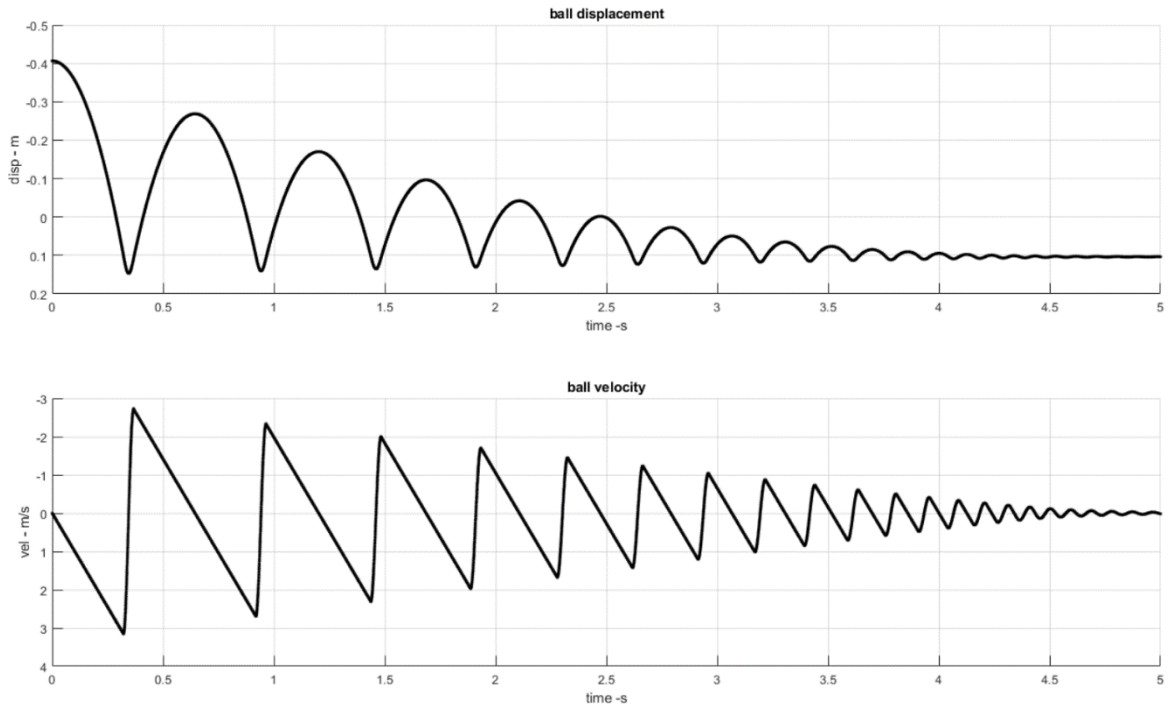
Figure 92 4.5 Psi Bouncing Simulation data
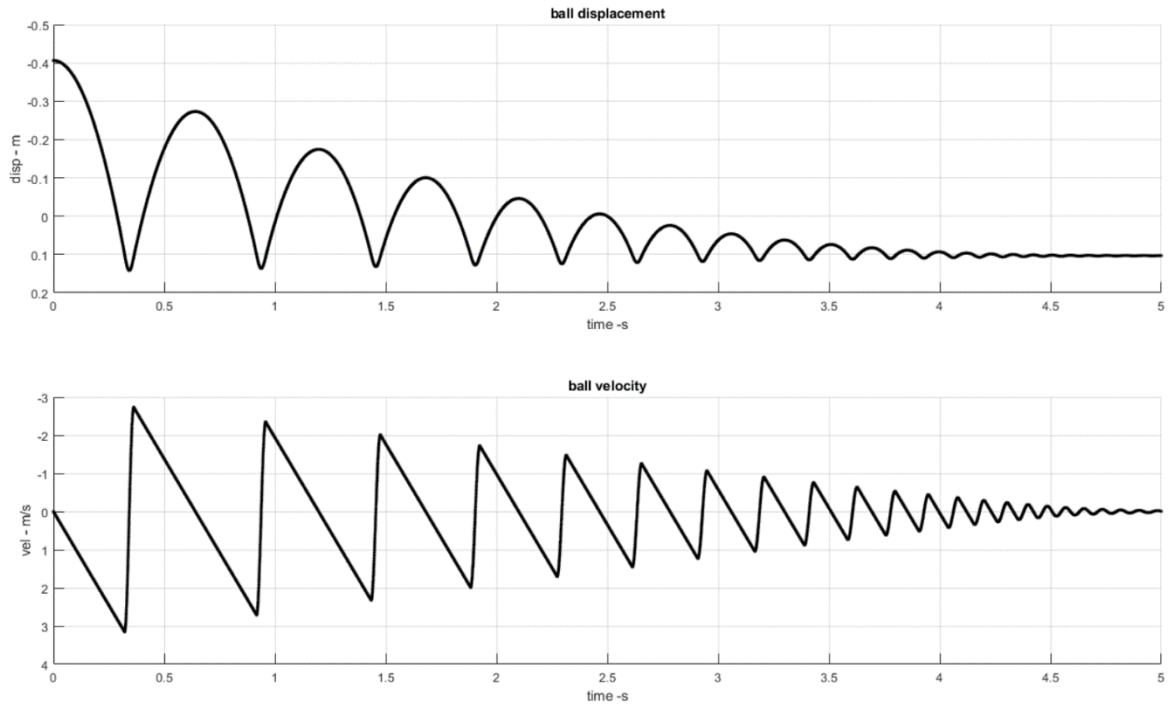
Figure 93 5 Psi Bouncing Simulation data

98
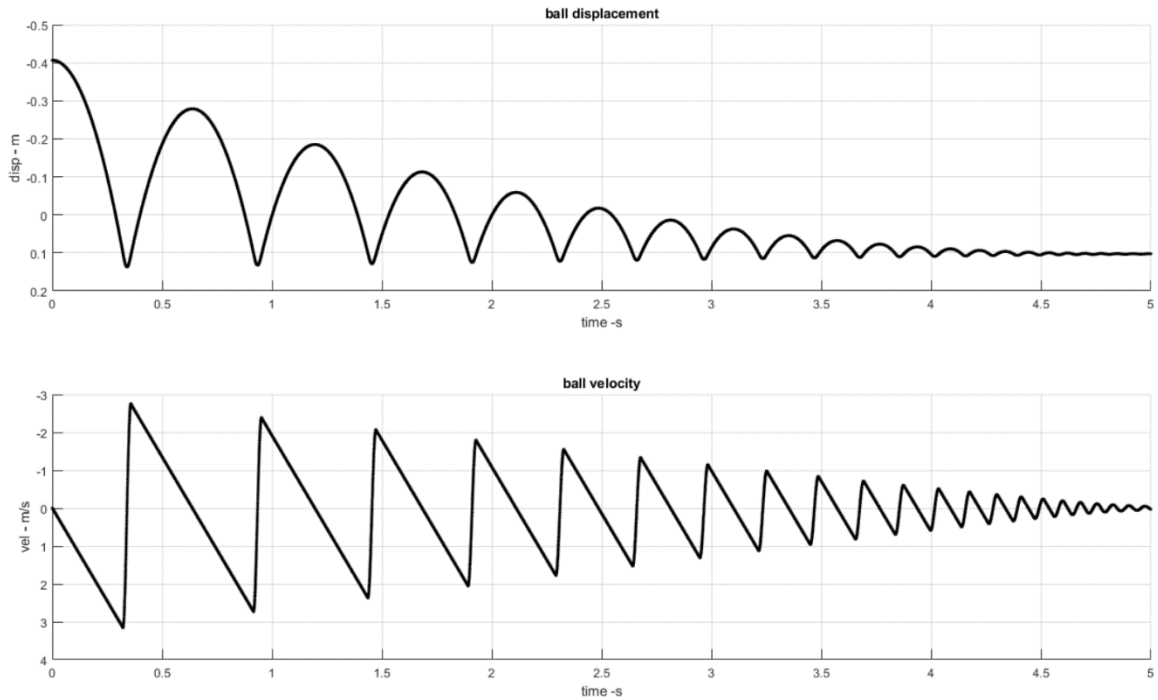
Figure 94 5.5 Psi Bouncing Simulation data

Next we compare the experimental results for motion and pressure data with the simulated motion. As pressure increases, it is clearly seen that the error between the measured data and the simulated data is increasing. At the end of each experimental run, the last few bounces have such a low pressure that the pressure sensor is not able to measure each bounce, likely leading to a smaller number of measured bounces that predicted.

The following table elaborates the Total time and number of bounces obtained through simulation.

Table 5 Simulated data

Pressure	Total Time	Number of bounces
2	3.15	12

99

2.5	3.2	12
3	3.3	12
3.5	3.4	13
4	3.75	15
4.5	4.5	18
5	4.75	19
5.5	5	25

Conclusion

From the results obtained in this chapter, it is clearly seen that with increasing ball pressure the coefficient of restitution is decreasing. The relationship between the pressure and the coefficient of restitution is of order 7 and is highly non-linear. Furthermore, the linear stiffness k increases with increasing ball pressure. The damping ratio was found to have an inverse relation with the pressure. For the robot to damp its bouncing, the system must reduce pressure using its pneumatic controller.

CHAPTER IX: DISCUSSION

Spherical robots are an alternative solution to the conventional wheeled vehicles with for rolling, although jumping, steering, and hopping can also be achieved. This style of robot has been developed in various forms for over a century. This history of evolution from J.L Tate's "toy" to the Samsung's "ballie" is commendable and clearly still underway. The advances in the micro-computers, wireless data -transfer, digital cameras, and high precision sensors offer new control solutions for dynamic operation. Adaptation of different mechanical and electro-mechanical driving mechanisms, sensors and materials has evolved across different mobility options such as pendulum drive, IDU, sliding mass, wind drive, etc. Each of these mechanisms may be well suited to different applications. With these advances, the spherical robot is evolving beyond a toy to serving as companions, guard robots or explorers. Areas of future work include the dynamics and control, path planning, interaction with humans and adapting to the environment.

Within the taxonomy of spherical robots, "RoboBall" is a BSR, 2 DOF pendulum drive system with ability to adapt and control its bouncing dynamics by changing internal pressure of the elastic ball. One axis is rolling continuously about a central axel, and the second can swing left or right for steering. The vertical bounding mode is affected by the pneumatic control and inertially stabilized pendulum is controlled using an IMU based feedback system. The machine manages its own stabilization, and can then be guided from onboard or offboard controllers. Based on this research of the design and dynamics of the ball's bounce, future versions will adapt pressure to best handle the terrain while smoothly accelerating and steering. Top speed is achieved on hard terrain at high ball pressure, with the pendulum lifted to a forward position. In this condition, the

ball accelerates to a terminal velocity where propulsive torque is balanced by rolling and aerodynamic drag.

The skin of the robot is a mixture of elastic exterior and the rigid endplates for supporting the rolling axis and allowing the robot to be a ship in the bottle design. The interface between the rigid and elastic surface to create a pressure vessel was non-trivial. Moreover, the interface should be air-tight for the robot holding up to 8 Psi of pressure. Three generation of ring deign iteration were performed for gripping the elastic bladder in the rings tested to as high as 10 Psi.

The material properties, pressure and thickness of the exterior shell both are the key factors that affect the operation of the robot. A static analysis was performed to see the variation of these parameters on the compression of the ball. The vertical compression of the ball drives the design of the radius of the pendulum to avoid contact with the ground. A couple things were observed from the analysis: (i) with increase in the thickness of the elastic shell the compression was reduced, (ii) with increase in the pressure the compression was also reduced. Future work will include trying different material for the bladder and the restraining cover for better results.

The development of internal pneumatic system was driven by the capability of the robot to change the internal pressure while driving. The system can change 2 psi gauge pressure within the ball. It consists of a compressor, 3 pressure tanks, 2 pressure sensors and a solenoid valve. The pneumatic control module is the controller and controls 3 stages of pressure change. The first stage is the idle mode where no action is taken i.e., compressor and the solenoid valve both are non-operational. The second stage pressurizes the ball, venting the tanks into the ball until the ball pressure achieves the desired level. The third stage uses the compressor to transfer ball air into the tanks, reducing ball air pressure to the desired level.

An experimental study was performed to observe bouncing of the ball as a function of the air pressure. The ball was repeatedly dropped from a 0.4 m height and data was recorded with internal pressure sensors and an external camera. The test ball held an internal mass to emulate the final RoboBall mass, and used the same rings and elastic shell design. Each experiment lasted until the ball stopped bouncing, recording the number of bounces and elapsed bounce time. This drop test was performed for multiple pressures, incrementing from 2 Psi gauge pressure to 5.5 Psi gauge pressure at 0.5 Psi increments. This experiment was conducted in safe laboratory environment, with a special built apparatus. The obtained pressure data was then analyzed with the impact model described in chapter VI.

The bouncing of the ball has two stages: In air and in contact with ground. Similarly, the total time elapsed after the drop includes time in the air and contact time. The analytic development assumes constant mass, pressure, linear stiffness, viscous damping, and coefficient of restitution. The model assumes a constant coefficient of restitution, and consequently a constant contact time, which does not match the experimental results and causes further errors in model correlation. This model does not include the effects of aerodynamic drag on the ball while in the air, which results in the higher simulated coefficient of restitution than otherwise would be predicted. This model gives an error of 50-60% in damping frequency from what independently is evaluated from the experimental data. Reconciling this large difference requires further study into the errors resulting from the underlying assumptions, namely, neglecting aero-dynamic drag and adopting a linear, fixed spring-mass-damper system, and overlooking the material properties of the elastic shell. Several observations can be made: (i) coefficient of restitution increases with increased pressure, (ii) coefficient of restitution increases with increasing linear stiffness, (iii) higher coefficient of restitution leads to lower damping ratio, and subsequently, a higher damping frequency.

Future exploration of different elastic shell materials and varying thickness will allow provide insight into the errors in this first order model and will help better understand the bouncing dynamics. Future impact models should take into account the neglected parameters such as aerodynamic drag, material friction between layers, and other nonlinearities in the system. After optimization and selection of the final shell material, the bouncing experiment should be conducted on different terrain, and at various speeds. This will build a data base for bouncing frequency associated with the pressure and the terrain. Being able to relate bounce dynamics with terrain and speed will enable the robot to detect and optimize its pressure for speed and control.

REFERENCES

[1] S.-S. Ahn and Y.-J. Lee, "Novel Spherical Robot with Hybrid Pendulum Driving Mechanism," *Advanced in Mechanical Engineering,* vol. 2014, 2014.

[2] M. Roozegar and M. Mahjoob, "Modelling and Control of a Non-Holonomic Pendulum-Driven Spherical Robot Moving on an Inclined Plane: Simulation and Experimental Results," *IET Control Theory and Applications,* vol. 11, no. 4, pp. 541-549, 2016.

[3] E. Kayacan, Z. Bayraktaroglu and W. Saeys, "Modeling and Control of a Spherical Rolling Robot: a Decoupled Dynamics Approach," *Robotica,* vol. 30, pp. 671-680, 2011.

[4] J. Kim, H. Kwon and J. Lee, "A Rolling Robot: Design and Implementation," *7th Asian Control Conference,* pp. 1474-1479, 2009.

[5] M. Nagurka and S. Huang, "A Mass-Spring-Damper Model of a Bouncing Ball," *International Journal of Engineering Education,* pp. 393-401, 2006.

[6] A. Georgallas, "The Coefficient of Restitution of Pressurized Balls: A Mechanistic Model," *Canadian Journal of Physics,* vol. 94, pp. 42-46, September 2015.

[7] M. Allen and B. Allen, "Temperature Dependence of Energy Loss in Gas-Filled Bouncing Balls," pp. 1-4, 8 February 2022.

[8] G. A. H. e. al., "An overview of wind-driven rovers for planetary," *43rd AIAA Aerospace Sciences Meeting and Exhibit, Reno,,* p. 0–13, 2005.

[9] J. Antol, P. Calhoun, J. Flick, G. Hajos, R. Kolacinski, D. Minton and R. &. P. J. Owens, "Low Cost Mars Surface Exploration: The Mars Tumbleweed," *National Aeronautics and Space Administration, Langley Research Center,* August 2003.

[10] A. B. e. al., "NASA/JPL Tumbleweed polar rover," in *Aerospace Conference,*, 2004 IEEE VOL1.

[11] J. A. e. al., "The NASA Langely mars tumbleweed rover prototype," *AIAA Aerospace Sciences Meeting and Exhibit,* vol. 64, 2006.

[12] M. 2. S. b. R. A. [Lyndon B.J. Bridgewater Final intern presentation.

[13] H. Xing, S. Guo, L. Shi, X. Hou, Y. Liu, H. Liu, Y. Hu, D. Xia and Z. Li, "A Novel Small-scale Turtle-inspired Amphibious Spherical Robot," *2019 IEEE/RSJ International Conference on Intelligent Robots and Systems (IROS),* pp. 1702-1707, 2019.

[14] A. &. F. A. &. U. W. &. A. H. Mazumdar, "A ball-shaped underwater robot for direct inspection of nuclear reactors and other water-filled infrastructure.," *IEEE International Conference on Robotics and Automation,* pp. 3415-3422, 2013.

[15] S. &. G. S. &. L. Z. Gu, "A highly stable and efficient spherical underwater robot with hybrid propulsion devices," *Autonomous Robots..*

[16] J. Matthews, "Development of the Tumbleweed Rover,," *NASA Jet Propulsion Laboratory,,* May 2003.

[17] M. Heimendahl, T. Estier and P. &. S. R. Lamon, "Windball," *Swiss Federal Institute,* 2004.

[18] J. A. Jones, "Inflatable robotics for planetary applications".

[19] T. Y. a. J. Suomela, "Ball-shaped robots," *Helsinki University of Technology.*

[20] R. D. A. S. a. A. T. K. Malandrakis, "Design and Development of a Novel," in *IFAC Symposium on Automatic Control in Aerospace,* , 2016.

[21] S. G. ·. S. G. ·. L. Zheng, "highly stable and efficient spherical underwater robot with hybrid," *Autonomous Robots,* p. 759–771, 2020.